Check for updates

Open-circuit voltage loss in perovskite quantum dot solar cells

Zijin Ding,[a] Saisai Li,[a] Yuanzhi Jiang, [iD][a] Di Wang[a] and Mingjian Yuan [iD] *[a,b]

Perovskite quantum dots are a competitive candidate for next-generation solar cells owing to their superior phase stability and multiple exciton generation effects. However, given the voltage loss in perovskite quantum dot solar cells (PQDSCs) is mainly caused by various surface and interfacial defects and the energy band mismatch in the devices, tremendous achievements have been made to mitigate the V_{oc} loss of PQDSCs. Herein, we elucidate the potential threats that hinder the high V_{oc} of PQDSCs. Then, we summarize recent progress in minimizing open-circuit voltage (V_{oc}) loss, including defect manipulation and device optimization, based on band-alignment engineering. Finally, we attempt to shed light on the methodologies used to further improve the performance of PQDSCs.

1 Introduction

Metal halide perovskites have drawn significant attention owing to their application in photovoltaic technologies, accompanied by a rapid increase in PCE from 3.8% to 25.7%.[1–5] Despite the stunning performance of perovskite solar cells, the notorious stability issues of bulk perovskites against temperature, humidity, and illumination are potential constraints that impede the further development of perovskite solar cells.[7–10] Perovskite quantum dots could be the ready solution to this dilemma. By leveraging the surface energy of quantum dots, the intrinsic stability of perovskites can be enhanced.[13–15] To date, the synthesis process is well-established to obtain high-quality perovskite quantum dots owing to the broad chemical diversity of the solvent system and capping ligands.[17–22] The combination of the peculiar synthetic method and layer-by-layer deposition decoupled the complicated crystallization kinetics from the deposition on the substrate and further pushed the PQDs toward application in solar cells.[27] In 2016, Luther *et al.* successfully harnessed the potential of perovskite quantum dots and, for the first time, reported the perovskite quantum dot solar cells (PQDSCs) with PCE exceeding 10%.[13] This study paved a new avenue for the perovskite solar cell and drew significant attention to the PQDSCs in the following years.[24,26,36–39]

The theoretical efficiency, based on Shockley–Queisser, is about 32% for a single-junction perovskite solar cell with a

bandgap of 1.5 eV.[43] Despite the widened bandgap for the size confinement effect and the high PLQY of PQDs, there is still an untapped opportunity to reduce the V_{oc} loss and improve the performance of PQDSCs. Owing to the complexity of the synthesis and post-treatment process, perovskite quantum dots usually have various surface defects, even the remnant of reactants, which possibly facilitate non-radiative recombination and cause voltage deficit.[16,45,46] In particular, the unclear surface chemistry, charge carrier dynamics, and inter-dot coupling make it more difficult to enhance charge carrier hopping between the dots. Moreover, a widely discussed interfacial recombination and energy level arrangement perplex the issue of V_{oc} loss.[48–52] Because of the excessive grain boundaries and interfaces introduced by layer-by-layer deposition, the PQD film inevitably contains many defects, intensifying non-radiative recombination. In addition, the unique surface properties increase the difficulty of manipulating the contact at the CTL/perovskite interface, thus causing severe degradation and deterioration of the charge transport at the interface.[47,53]

Considering the performance development of perovskite quantum dot solar cells, a significant amount of work is required to minimize the V_{oc} loss and boost the PCE towards the Shockley–Queisser limit. The aforementioned issues urgently need solutions to reduce the V_{oc} loss of PQDSCs, while a systematic review of the timely approaches to minimize the V_{oc} loss in PQDSCs is still lacking. In this review, we discuss representative studies on reducing the V_{oc} loss of a wide span of perovskite quantum dots with different compositions and bandgaps. We briefly introduce the theoretical background of detailed balance theory and the possible inducement of radiative recombination and non-radiative recombination loss. After that, we investigate the defect manipulation strategies of PQDs based on synthesis optimization and surface treatment. A series of studies on

[a]Key Laboratory of Advanced Energy Materials Chemistry (Ministry of Education), Renewable Energy Conversion and Storage Center (RECAST), College of Chemistry, Nankai University, Tianjin, 300071, P. R. China
[b]Haihe Laboratory of Sustainable Chemical Transformations, Tianjin, 300071, P. R. China. E-mail: yuanmj@nankai.edu.cn

surface engineering is reviewed. We attempt to give instructions on screening the appropriate capping ligands and purification solvents to reduce the non-radiative recombination of the PQDs. In Section 4, we emphasize interfacial modification and band alignment to boost charge carrier transport and reduce interfacial recombination. Some judicious approaches, including homojunction and heterojunction construction and charge transport material design, are summarized to minimize the V_{oc} loss. Finally, we raise some feasible methods to minimize the V_{oc} loss and anticipate the developed performance and further application for PQDSCs.

2   Voltage loss in PQDSCs

2.1   The mechanism of open-circuit voltage loss

The V_{oc} loss of perovskite quantum dot solar cells can be estimated based on detailed balance theory. In particular, the discrepancy between the bandgap and output V_{oc} in a real PSC comprises 3 parts (Fig. 1): (1) the difference between the S–Q limit and the bandgap (ΔE_1); (2) the radiative voltage loss ($\Delta E_2/q$), including $\Delta V_{oc, SC}$ (short-circuit loss term caused by the difference between J_{sc} and J_{sc}^{SQ}) and $\Delta V_{oc, rad}$; and (3) the non-radiative recombination caused voltage loss (ΔE_3).[57–59,62] We have

$$\begin{aligned} q\Delta V_{loss} &= E_g - qV_{oc} \\ &= (E_g - qV_{oc}^{SQ}) + (qV_{oc}^{SQ} - qV_{oc}^{rad}) + (qV_{oc}^{rad} - qV_{oc}) \\ &= \Delta E_1 + \Delta E_2 + \Delta E_3. \end{aligned}$$
$$(1)$$

According to the optoelectronic reciprocity theorem, ΔE_1 is assumed to be the energy difference between the bandgap and the S–Q limit V_{oc} caused by the isothermal losses and optical entropy generation.[60] This part of energy loss is usually in the range of 0.25–0.30 eV for a solar cell with an appropriate bandgap.[61] ΔE_1 can be expressed as a function of bandgap and temperature:

$$\Delta E_1 = E_g - k_B T \cdot \ln \frac{\int_{E_g}^{\infty} \phi_{AM1.5}(E)dE}{\int_{E_g}^{\infty} \phi_{BB}(E)dE},$$
$$(2)$$

where $\Phi_{AM1.5G}$ denotes the solar radiation spectrum with an air mass of 1.5 and Φ_{BB} for the black body radiation. This part of voltage loss is inevitable in all kinds of solar cells.
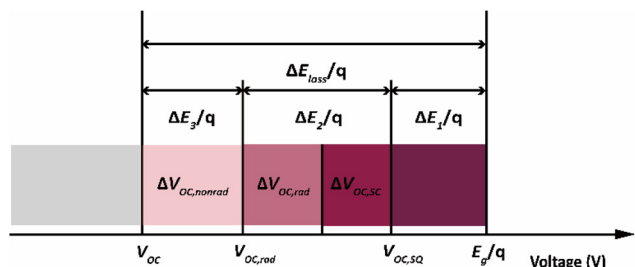

Fig. 1 Schematic illustration of the voltage loss in a practical solar cell.

ΔE_2 originates from the energy difference between the photoluminescent emission and the bandgap. The bandgap is regarded as a step function in S–Q theory, and the absorption of a practical solar cell is usually a function of the photon energy.[46] Hence, the EQE_{PV} is introduced to correct the expression for the ΔE_2, which indicates the ratio of the photons that generate the electric current of a solar cell held under short circuit conditions. ΔE_2 is calculated using the following equation:

$$\Delta E_2 = k_B T \cdot \ln \frac{\int_0^{\infty} EQE_{PV}(E) \cdot \phi_{BB}(E)dE}{\int_{E_g}^{\infty} \phi_{BB}(E)dE},$$
$$(3)$$

where ΔE_3 represents the non-radiative recombination loss, which is related to the defects in the practical solar cell. This part of the voltage loss is avoidable by optimizing the crystallinity of the light absorber and device structure. By ulteriorly plugging in EQE_{EL}, ΔE_3 is defined by the following equation:

$$\Delta E_3 = -k_B T \cdot \ln EQE_{EL}$$
$$(4)$$

$$EQE_{EL} = \frac{J_{0,rad}}{J_{0,rad} + J_{0,non-rad}},$$
$$(5)$$

where EQE_{EL} denotes the electroluminescence external quantum efficiency.

To directly quantify radiative loss (ΔE_2) and non-radiative loss (ΔE_3), several electrical, electro-optical, and optical methods have been developed to examine the origin of V_{oc} loss. As aforementioned, when a solar cell is on its radiative limit, the radiative limit dark saturation current ($J_{0, rad}$) can be calculated based on the optoelectronic reciprocity theory:

$$J_{0,rad} = q \int_0^{\infty} EQE_{PV}(E)\phi_{BB}(E)dE.$$
$$(6)$$

We can simply conclude from eqn (6) that the external quantum efficiency of a solar cell allows the determination of the radiative limit current, further the $V_{oc, rad}$ and ΔE_2. In a real solar cell, non-radiative loss comprises bulk recombination and surface recombination. The absolute PL is employed to disentangle these two kinds of energy loss, herein defined as $\Delta V_{oc, BNR}$ and $\Delta V_{oc, SR}$. $\Delta V_{oc, BNR}$ is usually regarded as the voltage loss caused by intrinsic defects that are usually electronically active and act as bulk recombination centers.[38] After the assembling of solar cells, the energetics and interfacial defects introduced by the contacts trigger the $\Delta V_{oc, SR}$. Under working conditions, electrons are excited from the valence band to the conduction band under irradiation, resulting in the redistribution of charge carriers. The Fermi level splits into the Fermi level of electrons (E_{Fn}) and holes (E_{Fp}). The $\Delta V_{oc, SR}$ is defined as the difference of quasi-Fermi level splitting ($\Delta E_F = E_{Fn} - E_{Fp}$) of perovskite before ($\Delta E_{F, bulk}$) and after contacts ($\Delta E_{F, contacts}$), which is expressed in the following equation:

$$\Delta V_{oc,SR} = \Delta E_{F,bulk} - \Delta E_{F,contacts} = \Delta E_{F,bulk} - qV_{oc}$$
$$(7)$$

In recent discussions, μ_{bulk} is quantified by the absolute photoluminescence spectra according to Würfel's generalized Planck's law:[111]

$$I_{PL}(E) = \frac{2\pi E^2 a(E)}{h^3 c^2} \frac{1}{\exp\left(\dfrac{E - \Delta E_F}{k_B T} - 1\right)}, \quad (8)$$

where $a(E)$ denotes the absorptivity related to photon energy E; with an assumption that the absorptivity of photons with energy above the PL maximum is regarded as unity, eqn (7) can be reduced to the following equation:

$$\ln \frac{I_{PL}(E)h^3 c^2}{2\pi E^2} = \frac{\Delta E_F}{k_B T} - \frac{E}{k_B T}. \quad (9)$$

After the above derivation (eqn (8) and (9)), the $\Delta E_{F,\ bulk}$ and $\Delta E_{F,\ contacts}$ can be deduced from the intercept by linear fitting of the high energy slope of PL spectra.[112]

After analyzing the step-by-step energy loss in the photoconversion process, we set up a holistic comprehension of the V_{oc} loss. In the next subsection, we discuss the specific voltage loss in a practical PQDSC, which we define as $(V_{oc,\ rad} - V_{oc})$.

2.2 Non-radiative recombination in PQDSCs

The detailed balance theory demonstrates that in PQDSCs, the non-radiative recombination triggered by the defect in the whole device and the energy level mismatch of different layers are the two main reasons that cause the V_{oc} loss. Despite the high defect tolerance and colloidal integrity of perovskite quantum dots, various issues arise in photovoltaic devices.[63] Owing to the peculiar synthesis method, cyclic purification, and deposition process, the surface ligands of PQDs are peeled off and cause some surface defects, which usually act as recombination channels.[46,64–66] The residual reactants serve as defects stemming from quantum dots. All latent defects can cause severe voltage loss in PQDSCs. To solve these problems, a more judicious synthesis protocol must be adopted. Moreover, capping ligands are another crucial element used in determining the quality of PQDs. Through delicate molecular design with multiple criteria, such as the ligand chemical hindrance and functional groups, the detachment and bond of the ligands could finally come to a dynamic equilibrium.[22,42,67,68] The ligand-exchange process on the as-deposited film is another factor that must be considered. A polar solvent is always employed as the ligand-removal agent without sacrificing the structural and phase stability of the quantum dots.[26,41] It is challenging to find appropriate anti-solvents that are the best of both worlds.

Apart from the voltage loss originating from the light absorber, interface recombination is almost a universal problem for all perovskite solar cells, which is usually caused by energy level mismatch and interfacial defects.[24,29,48,69] Generally, the unfavoured band structure between the light absorber and charge transport layers would cause insufficient charge transfer and block, thus generating charge carrier recombination at the interfaces. The ill-suited energy levels and large energy

offset would trigger band bending, thus narrowing the quasi-Fermi level splitting and lowering the V_{oc}. Although several strategies and efforts have been made to optimize the fabrication of PQDs, there is still room to reduce the voltage loss in
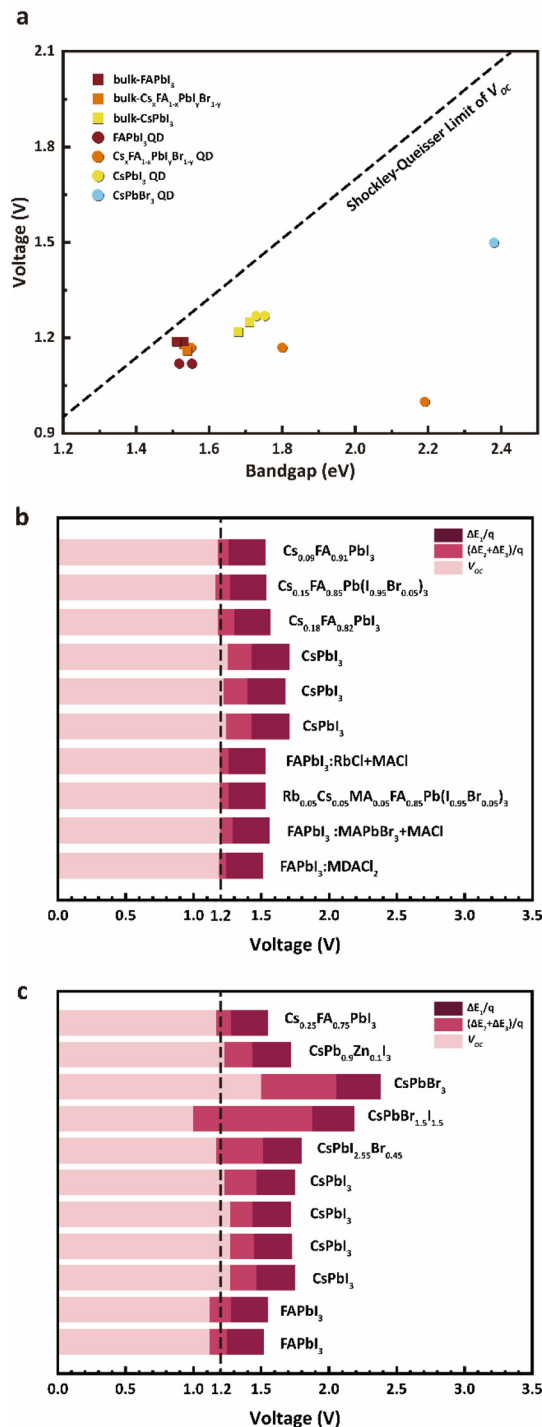

Fig. 2 (a) Comparison of open-circuit voltage *versus* bandgap of PQDSCs and their counterpart of bulk PSCs. Schematic illustration of (b) voltage loss with respect to the bandgap for bulk PSCs and (c) voltage loss with respect to bandgap for PQDSCs. The plots are based on the data listed in Table 1.[2–4,70–76]

PQDSCs based on the whole device level. In Fig. 2a–c, we compared the open-circuit voltage of the reported efficient PQDSCs and their counterparts in bulk PSCs against the Shockley–Queisser limit. It is shown that the A-site alloyed $Cs_{0.25}FA_{0.75}PbI_3$ QDs possess the smallest V_{oc} loss similar to the corresponding bulk perovskite solar cell with a similar bandgap, while others still suffer from a severe V_{oc} loss.[38] Throughout the developing history of the PSCs, it is evident that V_{oc} is regarded as the most challenging to improve. Because the fill factor (FF) highly depends on non-radiative recombination and interfacial contact, a decent V_{oc} guarantees high FF and good efficiency. Since Luther et al. first reported PQDSCs with efficiency exceeding 10%, to date, great efforts have been devoted to elevating the performance of the PQDSCs. A significant reduction in V_{oc} loss is achieved by multiple strategies, including but not limited to, optimizing the synthesis protocol, post-treatment, and device structure, which are discussed in the following sections.

3 Defect management of PQDs

The colloidal perovskite quantum dots are intrinsically defect-tolerant and always feature near-unity PLQY. However, after cyclic purification and layer-by-layer deposition process, multiple defects surely emerge that deteriorate the optoelectronic properties and cause V_{oc} loss. Hence, it is clear that the perfection of the synthesis protocol, ligand engineering, and post-treatment are prominent in rationalizing the surface defects of the QDs. Significant approaches to surface chemistry are summarized in the following subsection.

3.1 Synthesis protocol of perovskite quantum dots

The structural nature of QDs with a perovskite core wrapped in a ligand shell is important for studying capping ligands and surface properties. The capping ligands act as stabilizing surfactants and dominate the reaction path and the quality of the QDs. According to covalent bond classification theory, the extensive surface ligand database can be divided into X-type, L-type, and A-type categories.[65,77] X-type ligands are identified as one-electron donors that either interact with halide anion or Pb^{2+} and Cs^+ cations, and zwitterionic molecules, which interact with both. L-type ligands are two-electron donors that provide a lone pair of electrons for Pb^{2+}; z-type ligands are two-electron acceptors that accept a lone pair of electrons from the halide anions. The adhesion and functional groups varied from ligand to ligand, thus passivating various surface defects.

When we investigate the entire reaction of the synthesis process, the chemical equilibrium of the nucleation and growth stages significantly affects the properties. Qian et al. introduced a ternary precursor system and elucidated the relationship between the Pb/I ratios and QD optoelectronic properties (Fig. 3a).[6] After increasing the iodide input, the authors effectively dulled the iodide vacancies and achieved a champion V_{oc} of 1.248 V and a PCE of 13.12%. Chen et al. put forward a chemical stripping treatment, thus improving the orientation of PQD after being deposited into a solid film and

suppressing the intrinsic defect of the PQDs, as shown in Fig. 3b.[28] By judiciously optimizing the surface chemistry of the PQDs, the charge carrier transport is improved from dot-to-dot, and the charge carrier non-radiative recombination is inhibited. Considering the further post-synthesis process, the widely used OA/OLA ligands pair suffer from severe detachment. Based on the termination by CsX, PbX_2, and AX, the perovskite quantum dots are divided into three structural models, as shown in Fig. 3c and d.[42] The surface motif reveals a loose bind between the ammonium and bromide anions. The dynamic protonation and deprotonation processes of the OA ligand make PQDs even more fragile. These phenomena require urgent solutions and plenty of molecules with various carbon chain lengths and functional groups, and steric hindrances have developed over the past few years. Yang et al. prepared the $CsPbBr_3$ QDs with dodecylbenzene sulfonic acid as a surfactant (Fig. 3e).[55] This DBSA-assisted synthesis is convenient for later washing cycles because of the stronger adhesion of DBSA with lead atoms. In addition, phosphonate and other derivatives are also good options for preventing defect formation.

In general, it is difficult to stabilize a small perovskite nanocrystal with strong quantum confinement owing to its soft ionic nature and low lattice formation energy. The critical role of ligands in controlling the nucleation and growth of NCs appears to be an effective method for fabricating monodispersed and shaped uniform quantum dots with strong robustness. Moreover, size uniformity is crucial for a low-voltage deficit because a broad size distribution of PQDs causes the broadening of the bandtail states and aggravates the energetic disorder.[12,78,79]

Recently, Akkerman and co-workers proposed a "low ionic strength" reaction by introducing a weak coordination agent and a long-chain zwitterion to separate the nucleation and growth process in the precursor-to-QD conversion.[56] They proposed a facile strategy to adopt the trioctylphosphine oxide (TOPO) to form a stabilized TOPO: PbI_2 solution and apply the injected cesium-diisooctylphosphinate to trigger the formation of $PbBr_3^-$ ions, as depicted in Fig. 3f. The introduction of TOPO properly maintained the equilibrium between $PbBr_2$ and $[PbBr_3^-]$ and significantly retarded the reaction. The entire mechanism of this reaction is fully understood and evidenced by the in situ absorption spectra (Fig. 3g). The final obtained $CsPbBr_3$ nanocrystal is in a narrow size dispersion (Fig. 3h). It is worth mentioning that the versatility of this methodology is suited to all sorts of mainstream systems of perovskite.

The purification and isolation of PQDs is another necessary process to ensure that they are ready to be deposited onto the substrate. By cyclically rinsing the colloidal PQDs with various antisolvents, the residual reactants, by-products, and solvents can be removed. The most widely used MeOAc, first used by Luther,[13] is still an integral part of the purification process. However, this rinsing process leads to severe agglomeration caused by the excessive removal of ligands. For the implementation of an efficient photovoltaic device, the monodispersity and size uniformity of PQDs are significant prerequisites. Consequently, a more delicate and mild washing process must
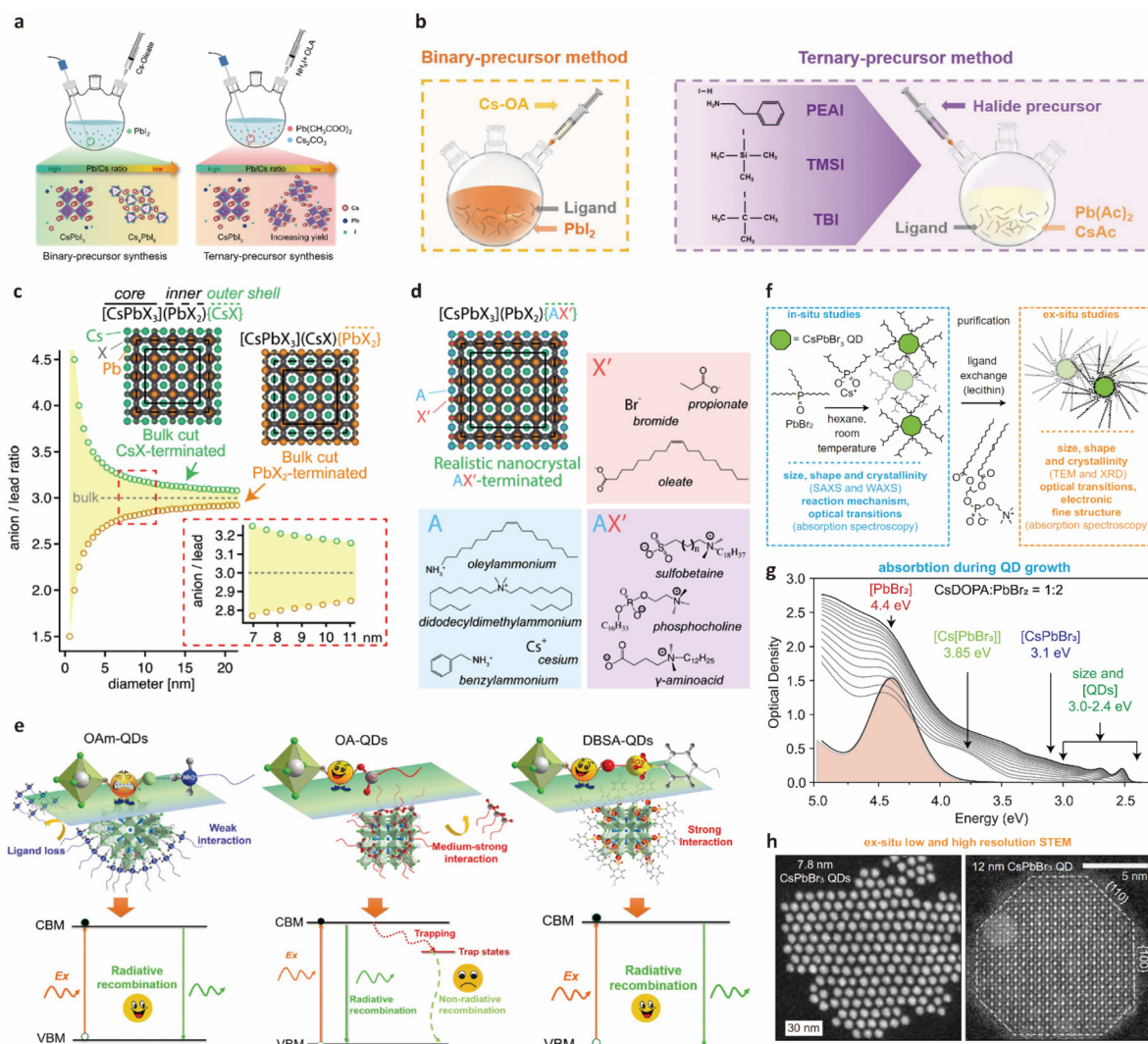
Fig. 3 Synthesis protocol optimization. (a) Schematic illustration of synthesis based on binary and ternary precursor. (a) Reproduced with permission from ref. 6, Copyright 2021, John Wiley and Sons. (b) Illustration of synthesis with binary and ternary-precursor method. (b) Reproduced with permission from ref. 28, Copyright 2022, John Wiley and Sons. (c) Size-dependent X/Pb ratio of cubic $CsPbX_3$ quantum dots with different surface motifs, where green, orange, and grey spheres represent Cs, Pb, and halide atoms, respectively. (d) The realistic termination of stabilized PQDs and some common ligands. (c and d) Reproduced with permission from ref. 42, Copyright 2019, American Chemical Society. (e) Ligand binding affinity with OA, OAm and DBSA and the corresponding exciton recombination process with the three ligand strategies. (e) Reproduced with permission from ref. 55, Copyright 2019, John Wiley and Sons. (f) Reaction scheme and overview of *in situ* and *ex situ* monitoring techniques used in the controlled synthesis of monodispersed QDs. (g) Evolution of the absorption spectra during the reaction. (h) STEM and HR-TEM images of the monodispersed spherical PQDs. (f–h) Reproduced with permission from ref. 56, Copyright 2022, American Association for the Advancement of Science.

be investigated to preserve stabilized PQDs with superior optoelectronic properties. Lim *et al.* attempted to improve the photovoltaic performance of all-inorganic $CsPbI_3$ PQDSCs through a first reported size selection *via* gel permeation chromatography (GPC).[12] The GPC is performed with the non-polar solvent toluene as the mobile phase and BioBeads as the stationary phase, as depicted in Fig. 4a. The tailored size selection improves the monodispersity of PQDs (Fig. 4b), thereby flattening the energy level and restraining the energy transfer between various bandgap compositions in the photovoltaic device. The V_{oc} of the target device is enhanced, with a champion parameter of 1.27 V and a PCE of 15.3% (Fig. 4c).

$FAPbI_3$ is an ideal candidate for efficient and stable photovoltaic devices; its optimal bandgap is promising for boosting performance toward the theoretical limit. However, the performance lags in the $FAPbI_3$ PQD solar cell, which is possibly attributed to the organic FA^+ cations, demonstrating softer binding with $[PbI_6]^{4-}$ cages than inorganic cations.[80] To customize the post-synthesis process, Xue *et al.* identified the solvents into three grades based on the polarity.[26] The polarity of the antisolvent determines its ability to peel off the insulated long-chain ligand without sacrificing the integrity of the QDs (Fig. 4d). After a systematic study of various solvents, they found that long-chain alcohols with electron-donating alkyl
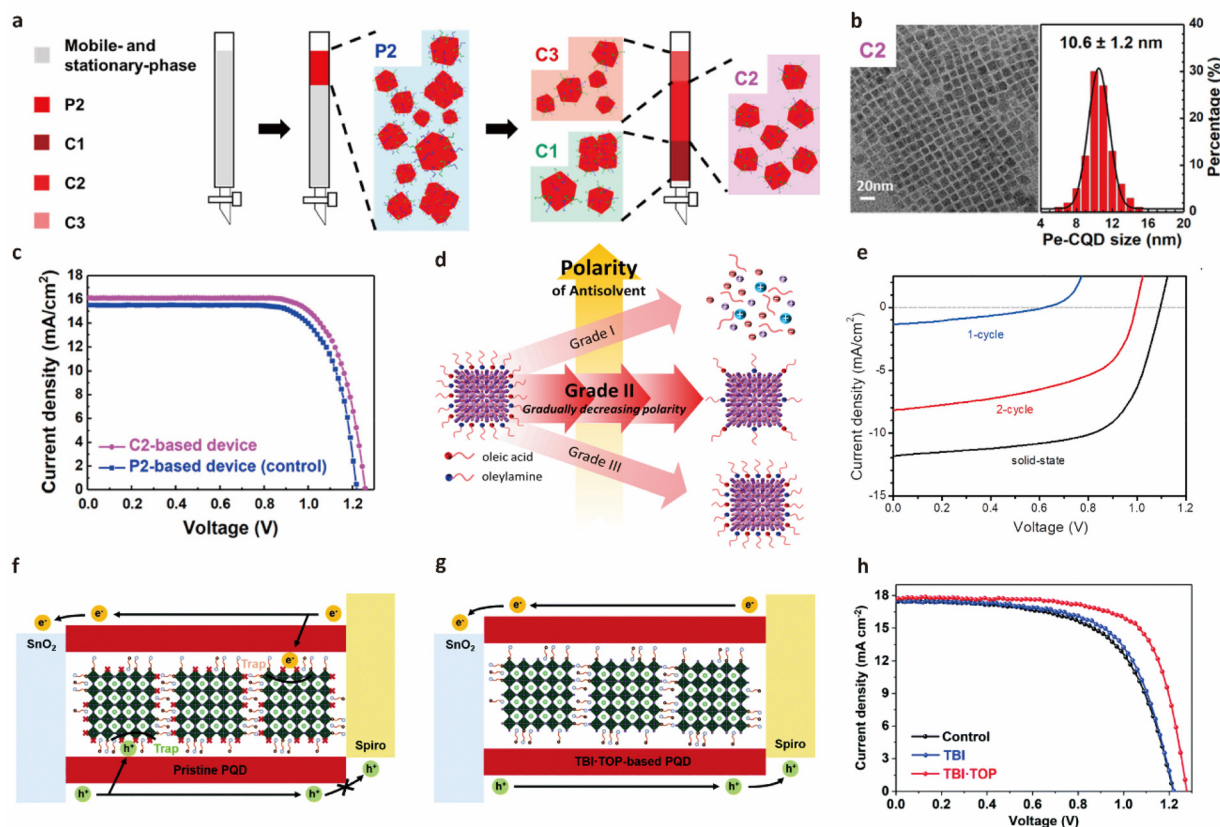
Fig. 4 Purification of the PQDs. (a) Schematic illustration of size selection *via* gel permeation chromatography. (b) HR-TEM images and the size distribution histogram of the best performed PQDs. (c) *J*–*V* curves of the control and GPC size selection-based PQDSCs. (a–c) Reproduced with permission from ref. 12, Copyright 2021, American Chemical Society. (d) Schematic illustration of strategy for rational design of solvent treatment for FAPbI$_3$ QDs. (e) *J*–*V* curves of the devices based on FAPbI$_3$ after cyclic purification. (d and e) Reproduced with permission from ref. 26, Copyright 2018, Elsevier. Schematic diagrams of the charge transport in (f) control device and (g) TBI·TOP-based devices. (h) Photovoltaic performances of control, TBI-based, and TBI·TOP-based devices. (f–h) Reproduced with permission from ref. 35, Copyright 2021, Royal Society of Chemistry.

chain can weaken the dipole of the C–O bond. In addition, the protic property can maintain the FA$^+$ protonated, thereby stabilizing the ionic lattice of the perovskite. Finally, the surface treatment is delicately designed by 2-step washing with solvents that possess gradient polarity. The *J*–*V* curve of the final PQD devices shows the highest V_{oc} of 1.10 V (Fig. 4e).

It has been proven that some of the raw ligands detach from the PQDs during the purification process, thus inducing halide vacancies. This issue attracted the attention of Jia *et al.* to replenish the halide vacancies, and they induced the *tert*-butyl iodide (TBI) and nucleophile trioctylphosphine (TOP) to trigger a nucleophilic substitution reaction and provided iodide for the X-site vacancies (Fig. 4f and g).[35] This novel strategy eliminated the uncoordinated Pb^{2+} on the surface of PQDs and greatly boosted the V_{oc} to 1.27 V (Fig. 4h).

3.2 Ligand exchange

Both purification and ligand exchange processes are intended to balance nicely the charge transport and integrity of the PQDs. The raw ligands of PQDs from the crude precursor are mainly insulating OAm/OA, which impairs charge transfer and

further operation of optoelectronic devices. Ligand exchange is designed to alter the density of the insulating ligands and replenish them with short-chain ligands to facilitate charge transport without compromising stability.

Based on the timing of ligand exchange, it can be divided into solution-state (*in situ*) and solid-state ligand exchange. Generally, solution-phase ligand exchange is more adequate for the dispersion of PQDs in solvents. A novel acid etching-driven ligand exchange is devised by Bi *et al.*[16] The HBr is induced into the precursor to etch imperfect [PbBr$_6$]$^{4-}$ octahedrons and remove excessive carboxylate ligands. Doodecylamine (DDDAM) and phenethylamine are induced for passivation and *in situ* ligand exchange, as depicted in Fig. 5a. This strategy successfully achieves the preparation of ultra-low defect density CsPbBr$_3$ PQDs, which is challenging for its small-size and labile nature. Additionally, Zhang *et al.* first developed the pseudo-solution-phase ligand exchange (p-SPLE) strategy by simply introducing short aromatic conjugated ligands into the antisolvent during the post-purification.[32] The aromatic short-chain ligands exhibit more effective electronic transfer *via* enhanced charge carrier deloca-
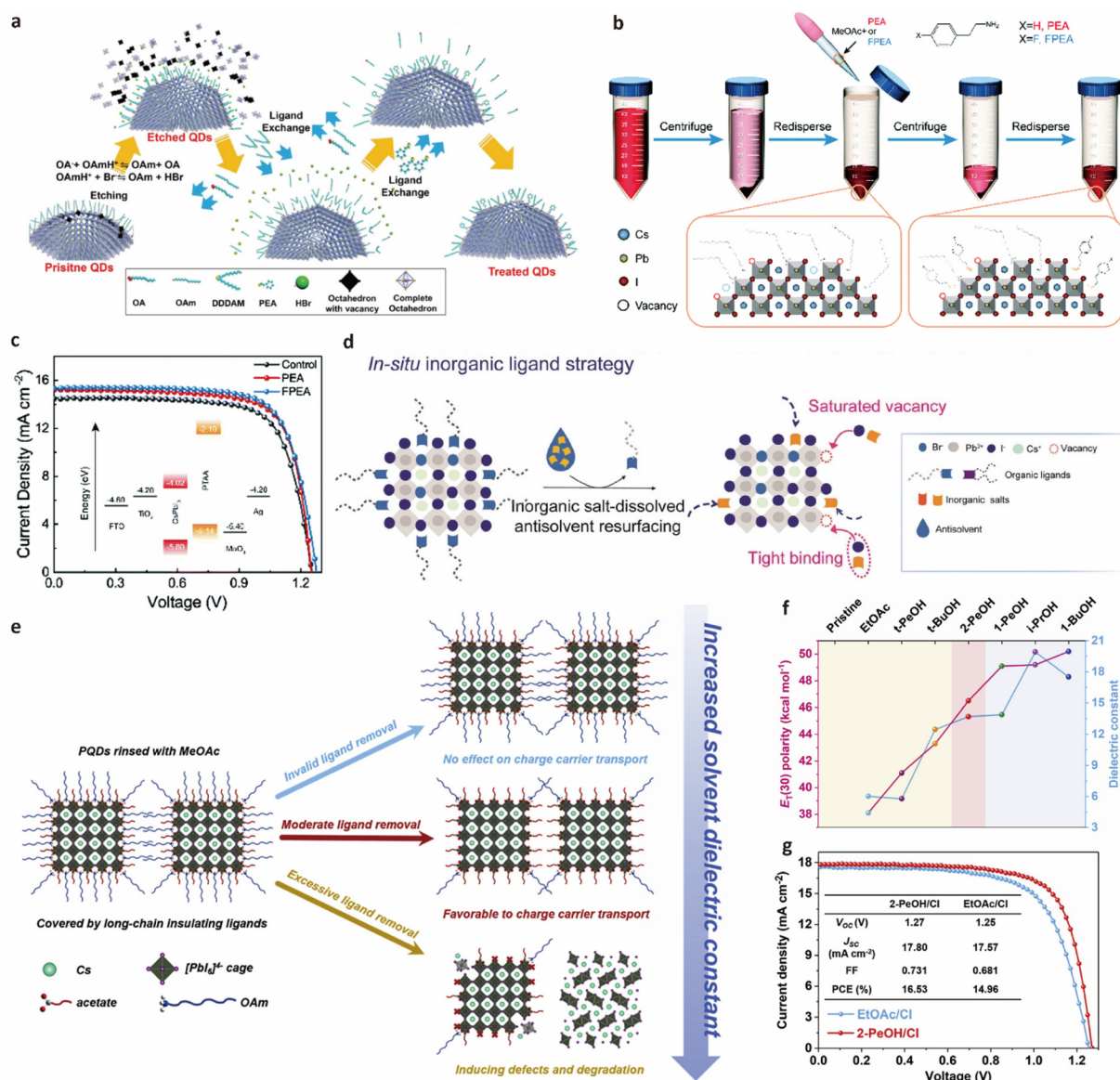
Fig. 5 Solution phase ligand exchange. (a) Schematic illustration of acid etching ligand exchange. (a) Reproduced with permission from ref. 16, Copyright 2021, John Wiley and Sons. (b) Schematic illustration of the *p*-SPLE strategy. (c) *J–V* curves of the control and *p*-SPLE PQDSCs and the energy level diagram. (b and c) Reproduced with permission from ref. 32, Copyright 2021, Royal Society of Chemistry. (d) The process of *in situ* inorganic ligand replenishment. (d) Reproduced with permission from ref. 34, Copyright 2022, John Wiley and Sons. (e) Effects of solvents with different dielectric constant upon PQDs. (f) Common antisolvents and their ET(30) polarity and dielectric constant. (g) Photovoltaic performance of EtOAc/CI-treated and 2-PeOH/CI-treated PQDSCs. (e–g) Reproduced with permission from ref. 41, Copyright 2022, Elsevier.

lization (Fig. 5b). Compared with the long-chain alkyl ligand, the steric effect also suppresses the distortion of $[PbI_6]^{4-}$ framework, thereby protecting the integrity of PQDs during ligand exchange. With well-passivated QDs, the open-circuit voltage is increased to 1.27 V with a PCE of 14.65%, as depicted in Fig. 5c. Inorganic ligands are also adopted in the *in situ* ligand replenishment to improve colloidal stability. Wang *et al.* introduced the inorganic ligand-EtOAc solution to *in situ* passivate the quantum dots. This strategy prevents the formation of defects with improved bandgap stability and resistance to ambient conditions (Fig. 5d).

The PQD solid is deposited with layer-by-layer or recently reported spray-coating methods.[81] Deposition is repeated 3–5 times to gain enough thickness of the absorbance layer. The solid-state ligand exchange renders the underlying layer insoluble and increases the packing density. To partially remove the surface ligand without destructing the PQD layer below, the deposited film is immersed into $Pb(NO_3)_2$ and MeOAc solution. In detail, the dissociative Pb^{2+} from $Pb(NO_3)_2$ combines with the halide ions and eliminates the deep-level defects of Pb vacancies and halide interstitials, thus improving the open-circuit voltage.[13] Wheeler *et al.* reveal that MeOAc

does not simply peel off the ligand through dissolution.[82] From a molecular level, they explain that the slow hydrolyzing of MeOAc with the aid of adventitious water produces acetic acid. Acetic acid then assists the ligand exchange by taking the place of the protonated oleate on the PQDs, leaving only the raw oleylammonium for further exchange. To thoroughly remove the native ligands, a post-treatment with a saturated solution of short-chain ligands in EtOAc is adopted to achieve ligand exchange. In general, the dielectric constant is considered an indicator for evaluating the polarity of the solvent. The higher the polarity, the stronger the electrostatic interaction between the solvent and surface ligands. However, the surface ligands or even the perovskite lattice are excessively peeled off if the interaction is too strong (Fig. 5e).[41,83–85] Considering the above criteria, a literature survey by Jia et al. points out 2-PeOH as a moderate solvent to facilitate the release of carboxyl ligands.[41] In Fig. 5f, they characterize the dual effect of the hydrogen bond acidity and polarity of the solvents. This extensive investigation eliminated 2-PeOH as an agent for solvent-mediated ligand exchange. Finally, a significant exaltation in the photovoltaic performance is observed, with up to 1.27 of V_{oc} (Fig. 5g).

Various short-chain ligands with a chemical formula of AX were decorated onto the PQDs after constructing a thick enough PQD solid. The cations are usually Cs, FA, phenethylammonium (PEA), and guanidinium (GA) cations with counterions, such as acetates, nitrates, and halides. The ligands with various cations and counterions are investigated to improve the photovoltaic performance of the solar cells with various mechanisms, thus enhancing the V_{oc}. It is reported that the hydrolysis product of MeOAc provides an acidic environment and causes hydroxide formation, in which both generate the band-tail and sub-bandgap trap states, resulting in the V_{oc} loss.[86,87] The acetates can address the issue mildly by a combination of passivating the A-site and halogen vacancies without introducing lattice distortion and defects. Using CsOAc, Ling et al. achieved a satisfying V_{oc} of 1.25 and an efficiency of 14.1%.[37] The surface matrix also plays an essential role in promoting the electronic interaction of QD solids. Ling et al. demonstrated a thermal annealing treatment with guanidinium thiocyanate triggering ligand exchange (LE-TA method), as illustrated in Fig. 6a.[88] The corresponding devices with such a strategy show an improved packing density and narrowed FWHM in steady-state PL spectra (Fig. 6b). The champion devices exhibit an open-circuit voltage of up to 1.25 V. Additionally, Chen et al. reported a surface surgery treatment with multidentate ethylene diamine tetraacetic acid (EDTA), as depicted in Fig. 6c.[11] The chelation and crosslink effects of EDTA suppress non-radiative recombination and facilitate inter-dot connectivity (Fig. 6d), improving the V_{oc} to 1.23 V. Despite the aforementioned ligands, zwitterionic ligands have also been demonstrated to concurrently passivate both A-site and X-site vacancies. Jia et al. used glycine as a dual-passivation ligand to diminish the recombination sites on the surface of PQDs (Fig. 6e).[31] Based on the SCLC measurement (Fig. 6g), the trap density of glycine-treated films

is significantly reduced. The dual passivation effect of amino acids improved the V_{oc} and PCE compared with $Pb(NO)_3$ treated devices, as shown in Fig. 6f.

4 Band alignment and device structure engineering

The record efficiency of QDSCs increases by up to 18.1%, while PQDSCs still suffer from a considerable V_{oc} loss. The investigation of recombination at or across the interface in PQDSCs remains obscure. Because the research on bulk perovskite solar cells has offered particular experience in tailoring the energy alignment and device structure, it can also be applied to PQDSCs for reference. This section presents various strategies for achieving a homogeneous energy landscape and eliminating interface recombination to harvest the full thermodynamic potential of PQDSCs.

4.1 Perovskite heterojunction and homojunction

The overmuch grain boundaries within the PQD film are regarded as an intractable issue because the charge carrier must traverse a number of interfaces before being extracted by the CTL. This prolonged tramp of charge carriers induces energy loss and impairs photovoltaic performance. To flatten the energy band structure, the concepts of perovskite heterojunction and homojunction within the PQD layer are commonly accepted. The perovskite heterojunction and homojunction are distinguished by whether there are compositional changes in the perovskite junction. The specific deposition method of QD layers brings convenience to building a heterojunction inside the light absorption layer.[89] Moreover, the compositional tunability and size confinement effect enable the fabrication of the QDs using a continuous bandgap.[38,90–92] By utilizing these abilities, the PQD layers with gradient bandgaps are integrated to facilitate a type-II energy landscape. In such a type-II band structure, the staggered heterojunction boosts the charge carrier transport and contributes to a high open-circuit voltage.[93,94] Zhao et al. exploited a series of PQDs and carried out a rational design of a charge-separating interface.[24] By performing ultraviolet photoelectron spectroscopy, they unveiled the anticipated type-II band structure with $Cs_{0.25}FA_{0.75}PbI_3/CsPbI_3$ quantum dots, as shown in Fig. 7a. The carrier dynamics are thoroughly studied with transient absorption, serving as a guideline for locating the junction spatially based on the charge carrier mobility and lifetime. The fast charge separation and well-designed structure simultaneously afford an enhanced open-circuit voltage and PCE (Fig. 7b). It is noteworthy that this concept provides a universal method for applying the heterojunction to various perovskite-based optoelectronics. Similarly, Li et al. reported a bilayer structure of $CsPbI_3/FAPbI_3$ (Fig. 7d).[29] The thermal annealing triggered cation exchange between the two components at the interface. The narrow-band gap $FAPbI_3$ QDs expand the light absorption and satisfy the band alignment, which concurrently improves the V_{oc} to 1.22 V (Fig. 7c).
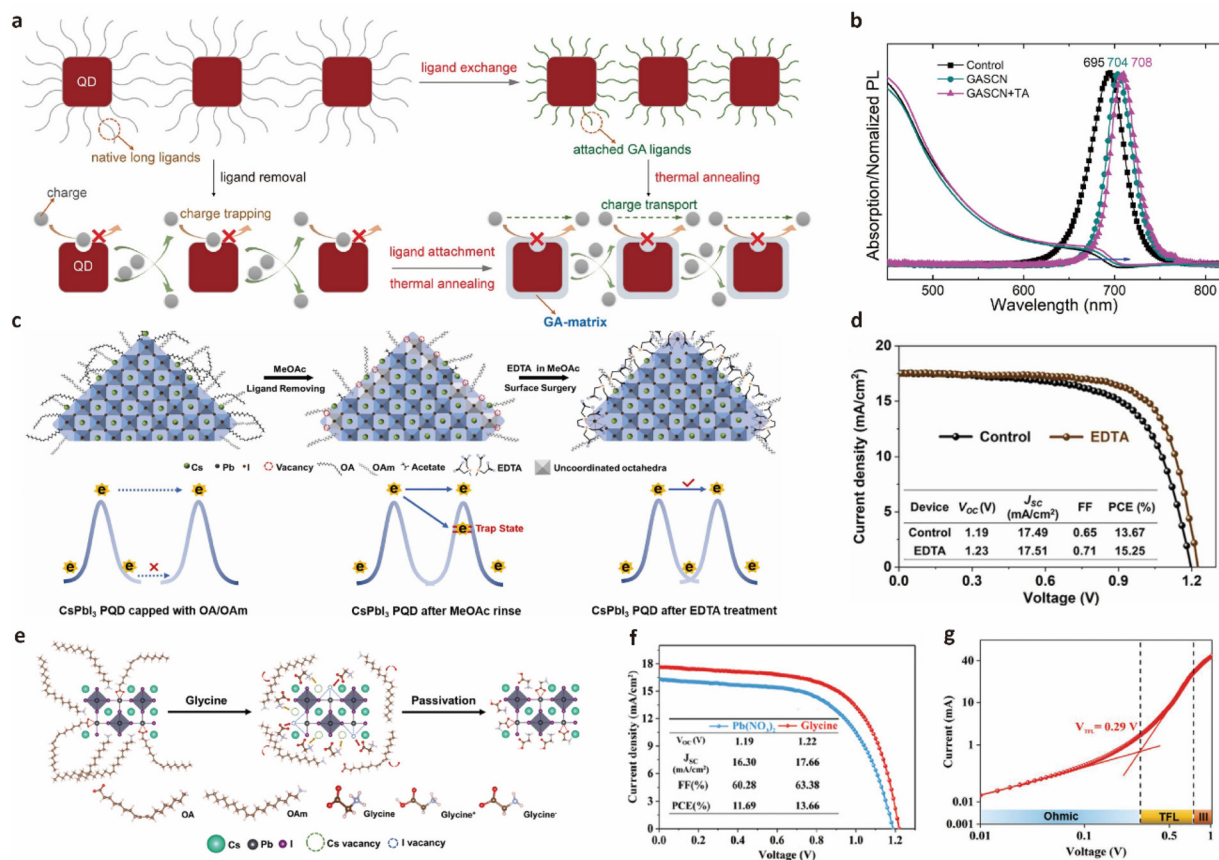
Fig. 6 Solid-state ligand exchange. (a) Schematic diagrams of the formation of GA-matrix capped CsPbI$_3$ PQDs using LE-TA method. (b) UV-vis absorption spectra and steady-state photoluminescence spectra of PQDs with different treatments. (a and b) Reproduced with permission from ref. 88, Copyright 2021, John Wiley and Sons. (c) Schematic diagram of the surface surgery treatments with EDTA molecules. (d) J−V curves of control and EDTA-passivated devices. (c and d) Reproduced with permission from ref. 11, Copyright 2022, Elsevier. (e) Dual passivation of Glycine. (f) Photovoltaic performances of Pb(NO)$_3$ and Glycine-treated PQDSCs. (g) SCLC measurement of the glycine-treated PQDSCs. (e−g) Reproduced with permission from ref. 31, Copyright 2020, John Wiley and Sons.

To construct a uniform energy landscape and passivation interlayer, Hu *et al.* constructed a hybrid interfacial architecture (HIA) by introducing PCBM into the CsPbI$_3$ QD layers.[33] The cascade-like energy levels, as illustrated in Fig. 7e, accelerate exciton dissociation and electron extraction at the interface, thereby suppressing interfacial recombination. The electrochemical impedance spectroscopy and fs-TA both corroborated that the photogenerated electrons are swiftly injected into the conduction band of the hybrid layer and then the ETL. With such an HIA structure, the open-circuit voltage is enhanced to 1.26 V (Fig. 7f). It is also impressive that this structure is compatible with the fabrication of flexible devices with extraordinary stability and mechanical flexibility.

After the removal of ligands, the charge carrier diffusion length is sacrificed, limiting the film thickness to 300–400 nm. The short carrier diffusion length and low extraction efficiency cause the charge carrier to be easily trapped by the defects, thus causing severe V_{oc} loss. Moreover, the insufficient film thickness makes the device suffer from poor J_{sc}. To overcome these problems, Zhang *et al.* developed a homojunction struc-

ture with a charge transfer doping strategy.[44] This P/N homojunction broadened the depletion region, concurrently improving extraction efficiency and reducing charge carrier recombination. The dopant F6TCNNQ could achieve slight *p*-doping after being attached to the PQDs, thus introducing a built-in electric field (Fig. 7g). This method incorporated technical feasibility to establish one μm-thick film with an efficient charge carrier, which provides a helpful guideline for enhancing PQDSCs.

In addition to the compositional regulation-based heterojunction, Yuan *et al.* devised a homojunction by tuning the bandgap based on the size-dependent quantum confinement effect (Fig. 7h).[54] The preparation of QDs of various sizes is accomplished by adjusting the temperature of the hot-injection method. Thereafter, the as-fabricated QDs are sequentially deposited, and the bandgap gradually widened from the bottom to the top. The homojunction with a sloping pattern of both the conduction and valence bands is conducive to drifting the charge carriers. As shown in Fig. 7i, a V_{oc} of 1.26 V evidenced suppressed recombination with the concept of homojunction.
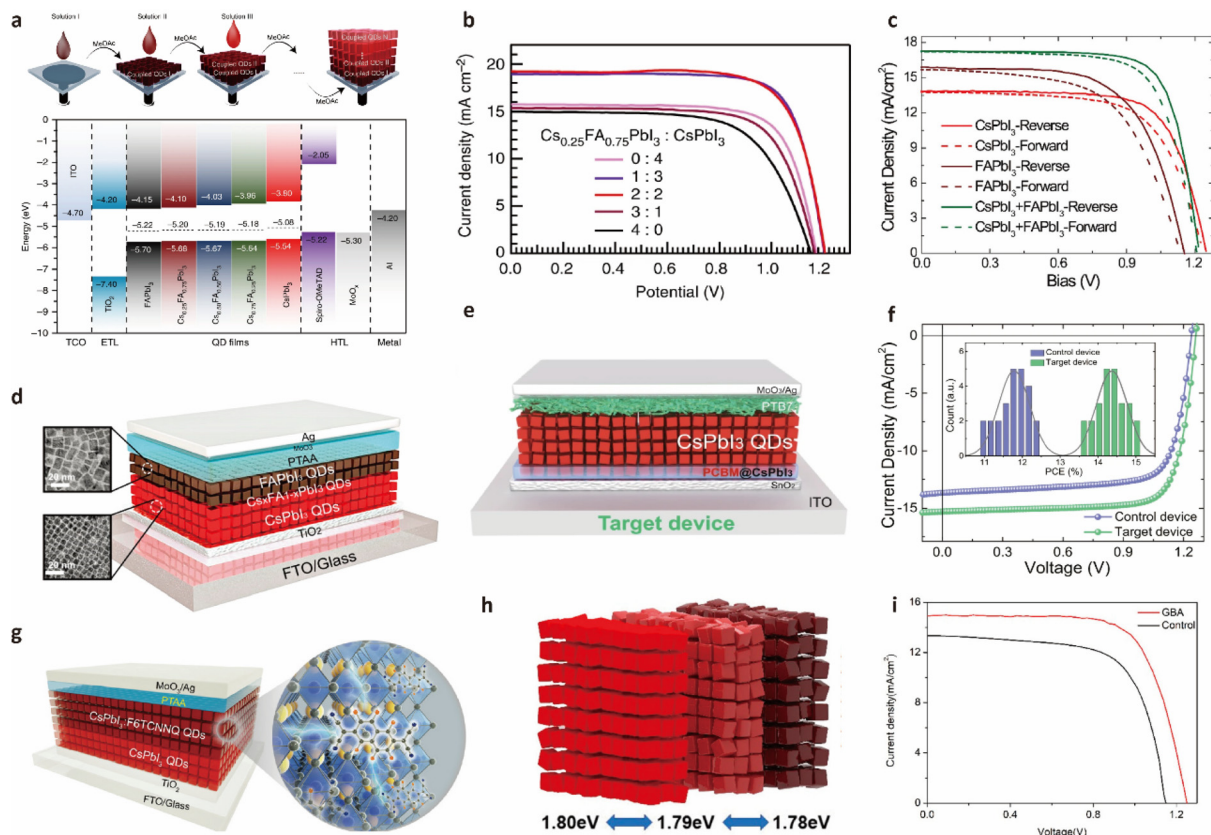
Fig. 7 Perovskite heterojunction in PQDSCs. (a) Energy band structure of different composition. (b) *J–V* curves of PQDSCs with different thickness ratios. (a and b) Reproduced with permission from ref. 24, Copyright 2019, Springer Nature. (c) *J–V* curves of PQDSCs with CsPbI₃, FAPbI₃ and CsPbI₃ + FAPbI₃. (d) Schematic diagram of α-CsPbI₃/FAPbI₃ bilayer structure-based PQDSCs. (c and d) Reproduced with permission from ref. 29, Copyright 2019, American Chemical Society. (e) Device structure of PQDSCs with interfacial structure. (f) Photovoltaic performances of PQDSCs with PCBM@CsPbI₃ interlayer. (e and f) Reproduced with permission from ref. 33, copyright 2021, Springer Nature. (g) Schematic illustration of P/N homojunction device with CsPbI₃ and F6TCNNQ : CsPbI₃. (g) Reproduced with permission from ref. 44, Copyright 2022, John Wiley and Sons. (h) The gradient-band alignment homojunction structure. (i) *J–V* characteristic of PQDSCs based on control and GBA structure. (h and i) Reproduced with permission from ref. 54, copyright 2021, American Chemical Society.

4.2 Interfacial modification

It is often said that the interface is the device, while PQDSCs are complicated systems that comprise diverse surfaces and interfaces. To alleviate severe interfacial recombination, interfacial passivation plays a solid foundation in boosting the photovoltaic performance of PSCs.[113] The weak dot-to-dot coupling remains a significant obstacle to the transport and separation of photogenerated carriers.[95] Because extraction and recombination are two competitive processes, it is challenging to achieve a good V_{oc} with an unvarnished device. By taking advantage of the conjugated molecule 2,2′-[[6,6,12,12-tetrakis(4-hexylphenyl)-6,12-dihydrodithieno[2,3-*d*:2′,3′-*d*′]-*s*-indaceno[1,2-*b*:5,6-*b*′]dithiophene-2,8-diyl]bis[methylidyne(3-oxo-1*H*-indene-2,1(3*H*)-diylidene)]]bis[propanedinitrie] (ITIC), Xue and coworkers demonstrated an interfacial charge driver that provides a driving force for promoting charge separation.[25] The deposition method is depicted in Fig. 8a. The hybrid heterointerface between QDs and organic molecules decreased the electron–hole pair lifetime and guaranteed

better electron delocalization. From the perspective of the band structure, the ITIC is only in contact with the ETL to avoid an energy level mismatch and charge recombination. Compared with the unvarnished device, the target device achieved a better V_{oc} of 1.10 V and a PCE of 12.7% based on FAPbI₃ QDs. The problems above were also encountered by Wang *et al.* To promote the conductivity and charge transport of the QD film, they use high mobility μ-Graphene sheets to crosslink the CsPbI₃ QDs.[30] As shown in Fig. 8c, the μGR supports a more effective extraction of the electrons with an appropriate energy level and enhances the resistance of QDs against humidity. In general, the device based on the μGR crosslinked CsPbI₃ QDs presents an increased V_{oc} from 1.16 V to 1.18 V and a PCE of 11.64% (Fig. 8d).

Owing to the large surface energy difference between the QDs and polymers, the contact between the QD film and CTL is not ideal.[96] The incompatibility between the charge transport materials and QDs causes incomplete coverage of the QD layers or even polymer aggregation, which is detrimental to charge transport at the interface. Ji *et al.* addressed this issue
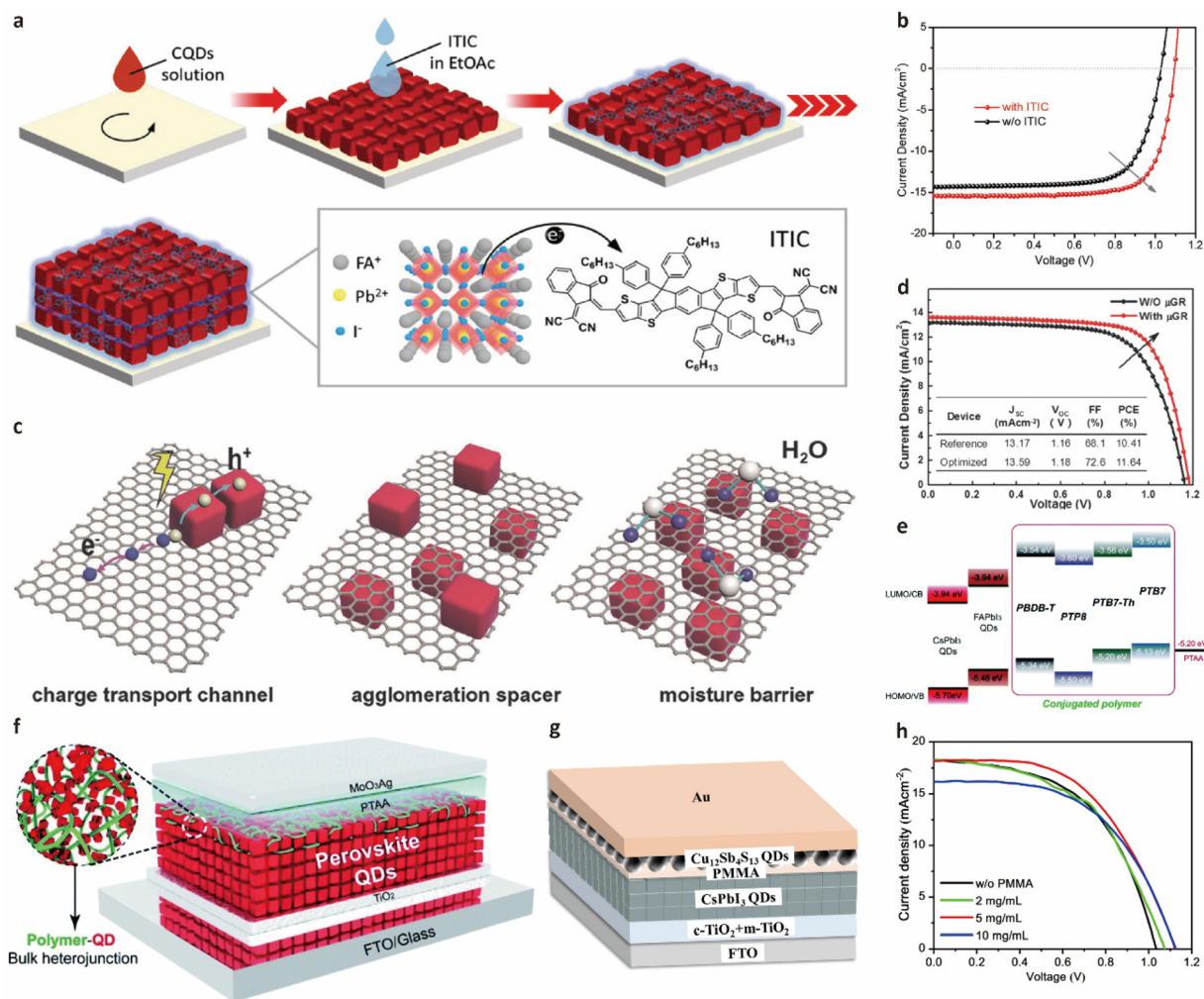
Fig. 8 Interfacial modification for PQDSCs. (a) FAPbI$_3$ QDs/ITIC film fabrication. (b) J–V curves of PQDSCs with and w/o ITIC. (a and b) Reproduced with permission from ref. 25, Copyright 2019, John Wiley and Sons. (c) Schematic illustrations of charge transport in μ-GR/CsPbI$_3$ QDs-based PQDSCs. (d) Photovoltaic performance of μ-GR/CsPbI$_3$ QDs-based PQDSCs. (c and d) Reproduced with permission from ref. 30, Copyright 2018, John Wiley and Sons. (e) Band structure of PQDs and conjugated polymers in this study. (f) Device structure of PQDSCs with bulk heterojunction structure. (e and f) Reproduced with permission from ref. 40, copyright 2020, John Wiley and Sons. (g) Device structure of PQDSCs with PMMA interlayer. (h) J–V characteristic of PQDSCs with different concentrations of PMMA. (g and h) Reproduced with permission from ref. 47, Copyright 2021, Elsevier.

with an interfacial bulk heterojunction (BHJ), as shown in Fig. 8f.[40] The interfacial modifier is developed with a polymer-QD hybrid layer, which features an aligned energy level and bridge-like function. The modified device structure indicates a synergistic suppression of bimolecular recombination and interfacial trap-assisted recombination, thus diminishing the V_{oc} loss.

Particular emphasis is also placed on the interfaces between the perovskite layer and the CTL because the interfacial defects are accountable for the V_{oc} loss. Wei *et al.* utilized the insulating poly (methyl methacrylate) (PMMA) as a buffer layer between the CsPbI$_3$ QDs film and the inorganic HTL Cu$_{12}$Sb$_4$S$_{13}$ QDs.[47] It is verified in this study that PMMA acts as an interfacial modifier and reduces the interface defects responsible for the monomolecular recombination

process. The V_{oc} exhibited an improvement from 1.04 to 1.14 after the intercalate of PMMA (Fig. 8h).

4.3 Charge transport layer

Apart from the preparation of well-passivated light absorbers, the energy levels of the light absorber and charge transport layers (CTL) dominate the electronic process occurring in the whole device.[97] The energy level mismatch between the PQD solids and CTLs narrows the quasi-Fermi level splitting, thus leading to a V_{oc} deficit. Concretely, it is reported that interfacial non-radiative recombination often exponentially increases in the case of considerable energy offset at the interface.[48] To minimize the V_{oc} loss, the suitability between different charge transport materials and perovskite quantum dots is considered.

To avoid recombination, an ideal CTL should function as a charge extraction layer with high mobility while blocking the opposite charge back-transfer. Among these versatile charge transport materials, mesoporous TiO_2 is known to feature a large contact surface with perovskite, which is beneficial for charge transport and separation. However, the surface inhomogeneity of m-TiO_2 and PQDs negatively affects the contact. To demonstrate the better incorporation of QDs into mesoporous TiO_2, Chen et al. explored a novel approach using CsOAc as the surface modification agent (Fig. 9a).[53] The CsOAc-modified surface of TiO_2 lowered the adsorption energy, while the Cs-rich surface can also passivate the PQDs. As shown in Fig. 9b, the outcome of the devices based on m-TiO_2 exhibits a PCE exceeding 14%. The SnO_2 nanoparticle and polycrystalline film have provided a solid foundation for achieving the cutting-edge efficiencies of perovskite solar cells. Recently, Lim et al. found that the photoactivity and hydrophilicity of TiO_2 make $CsPbI_3$ QDs suffer from a severe phase transition (Fig. 9c).[98] They systematically investigated the impact of

various ETLs on the stability and demonstrated the replacement of TiO_2 with Cl-passivated SnO_2 quantum dots. Owing to the hydrophobic characteristic and band alignment (Fig. 9d), an enhancement of V_{oc} and stability are observed.

Studies on the hole transport layer have also been widely carried out. Spiro-oMeTAD is a major competitive candidate for achieving the high efficiency of perovskite solar cells. However, the troublesome doping mechanism limited the inherent stability of Spiro-oMeTAD. The excessive tBP inside the solid film undergoes slow evaporation and results in pinholes within the HTL.[99,100] The agglomeration and migration of Li_xO_y are detrimental to the homogeneity of the whole film.[101–103] The degradation over time and the de-doping process remain unexplained; hence, the need for a prompt solution arises.[104] To better comprehend the problem and offer a solution, Yuan et al. employed a series of polymeric hole transport materials instead of Spiro-OMeTAD.[23] The conjugated HTM does not need a sophisticated doping process,
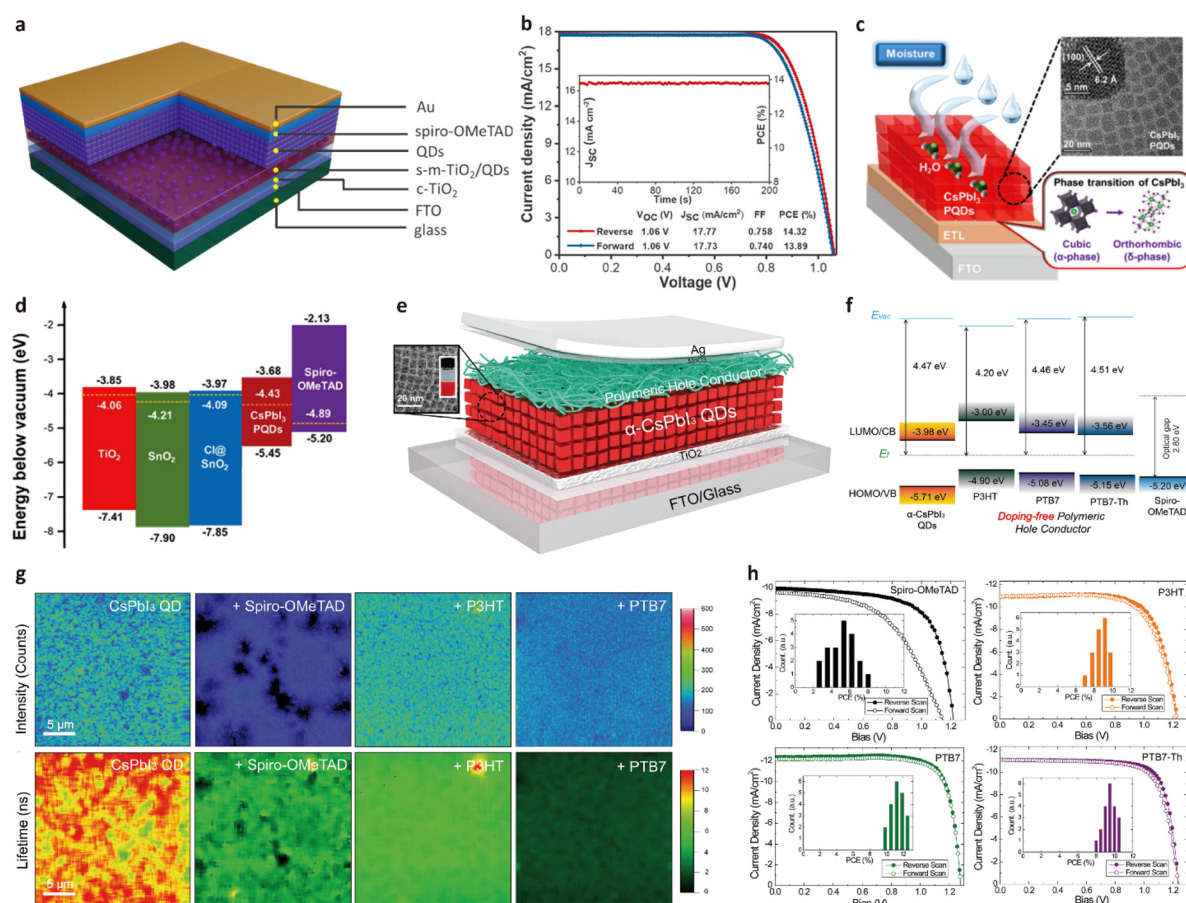

Fig. 9 Charge transport layers in PQDSCs. (a) $CsPbI_3$ PQDSCs with mesoporous structure. (b) Photovoltaic performance of the champion device. (a and b) Reproduced with permission from ref. 53, Copyright 2021, American Chemical Society. (c) Device structure of PQDSC with ETL engineering. (d) Energy band diagram of $CsPbI_3$-PQD solar cells. (c and d) Reproduced with permission from ref. 98, Copyright 2021, American Chemical Society. (e) Schematic diagram of the device structure. (f) Band structure of $CsPbI_3$ PQDs and polymeric hole transport materials. (g) Time-resolved confocal imaging of $CsPbI_3$ QD films and HTMs. (h) Photovoltaic performances of PQDSCs with different HTMs. (e–h) Reproduced with permission from ref. 23, Copyright 2018, Elsevier.

Table 1 Summary of photovoltaic performance and voltage loss in PQDSCs

Composition	Device structure	Bandgap (eV)	PCE (%)	J_{sc} (mA cm^{-2})	V_{oc} (V)	FF (%)	Voltage loss ($V_{oc}^{rad} - V_{oc}$) (V)	Ref.
CsPbI$_3$	FTO/TiO$_2$/PQDs/spiro-OMeTAD/MoO$_x$/Al	1.75	10.77	13.47	1.23	0.65	0.235	13
CsPbI$_3$	FTO/TiO$_2$/PQDs/spiro-OMeTAD/MoO$_x$/Al	1.77	13.43	14.34	1.2	0.78	0.284	36
CsPbI$_3$	FTO/c-TiO$_2$/m-TiO$_2$/PQDs/spiro-OMeTAD/Au	1.74	14.32	17.77	1.06	0.75	0.396	53
CsPbI$_3$	FTO/MoO$_3$/Ag/SnO$_2$/PQDs/spiro-OMeTAD/MoO$_3$/Ag	1.77	14.5	16.40	1.23	0.72	0.254	98
CsPbI$_3$	FTO/TiO$_2$/PQDs/polymeric HTL/MoO$_x$/Ag	1.73	12.55	12.39	1.27	0.80	0.176	23
CsPbI$_3$	ITO/SnO$_2$/PQDs/spiro-OMeTAD/Ag	1.74	13.66	17.66	1.22	0.64	0.236	31
CsPbI$_3$	ITO/SnO$_2$/PQDs/spiro-OMeTAD/Ag	1.76	16.21	17.71	1.27	0.72	0.204	35
CsPbI$_3$	ITO/SnO$_2$/PQDs/spiro-OMeTAD/Ag	1.75	15.25	17.49	1.19	0.65	0.275	11
CsPbI$_3$	FTO/TiO$_2$/PQDs/PTAA/MoO$_3$/Ag	1.72	13.69	14.53	1.25	0.75	0.189	6
CsPbI$_3$	ITO/SnO$_2$/PQDs/spiro-OMeTAD/Ag	1.72	16.25	17.73	1.23	0.74	0.207	28
CsPbI$_3$	FTO/NiO/PQDs/spiro-OMeTAD/MoO$_x$/Ag	1.72	15.3	16.10	1.27	0.75	0.167	12
CsPbI$_3$	FTO/TiO$_2$/QDs/spiro-OMeTAD/Au	1.80	11.2	14.40	1.11	0.70	0.402	81
CsPbI$_3$	ITO/SnO$_2$/PQDs/spiro-OMeTAD/Ag	1.76	16.53	17.40	1.27	0.73	0.204	41
CsPbI$_3$	FTO/TiO$_2$/PQDs/spiro-OMeTAD/MoO$_x$/Ag	1.72	13.3	15.21	1.18	0.74	0.257	86
CsPbI$_3$	FTO/TiO$_2$/PQDs/PTAA/MoO$_x$/Ag	1.72	15.21	15.85	1.25	0.77	0.187	88
CsPbI$_3$	FTO/TiO$_2$/PQDs/PTAA/MoO$_x$/Ag	1.76	15.33	16.34	1.26	0.74	0.210	106
CsPbI$_3$	ITO/SnO$_2$/PCBM-PQDs/PTB7/MoO$_3$/Ag	1.76	15.1	15.20	1.26	0.78	0.214	33
CsPbI$_3$	FTO/TiO$_2$/PQDs/spiro-OMeTAD/Au	1.74	13.47	15.5	1.18	0.73	0.276	91
CsPbI$_3$	FTO/TiO2/PQDs/spiro-OMeTAD/MoO$_x$/Al	1.72	14.74	16.37	1.2	0.75	0.237	90
CsPbI$_3$	FTO/TiO$_2$/PQDs-µGR/PTAA/Au	1.74	11.4	13.59	1.18	0.73	0.276	30
CsPbI$_3$	FTO/TiO$_2$/PQDs/PTAA/MoO$_x$/Ag	1.76	13.8	15.10	1.22	0.75	0.254	40
CsPbBr$_3$	FTO/c-TiO$_2$/PQDs/spiro-OMeTAD/Au	2.38	5.208	5.60	1.5	0.62	0.554	105
Heterojunction	FTO/TiO$_2$/PQDs/PCBM/Ag	—	13.2	14.90	1.25	0.71	—	54
Homojunction	FTO/TiO$_2$/n-CsPbI$_3$ QDs/p-CsPbI$_3$ QDs/PTAA/MoO$_3$/Ag	—	15.29	17.12	1.25	0.71	—	44
Bilayer	FTO/TiO$_2$/PQDs/PTAA/MoO$_x$/Ag	—	15.6	17.26	1.22	0.74	—	29
Heterostructure	ITO/TiO$_2$/PQDs/spiro-OMeTAD/MoO$_x$/Al	—	17.39	18.91	1.20	0.76	—	24
Cs$_{0.25}$FA$_{0.75}$PbI$_3$	ITO/SnO$_2$/PQDs/spiro-OMeTAD/Au	1.55	16.6	18.30	1.17	0.78	0.108	38
CsPb(I$_{0.05}$Br$_{0.95}$)$_3$	FTO/TiO$_2$/PQDs/spiro-OMeTAD/MoO$_x$/Al	2.25	1.92	2.36	1.39	0.59	0.542	90
CsPbBr$_{1.5}$I$_{1.5}$	FTO/c-TiO$_2$/PQDs/spiro-OMeTAD/MoO$_3$/Ag	2.19	7.945	11.35	1.00	0.70	0.876	107
CsPbI$_{2.55}$Br$_{0.45}$	FTO/m-TiO$_2$/PQDs/spiro-OMeTAD/Au	1.80	12.88	15.47	1.17	0.71	0.342	108
CsPb$_{0.9}$Zn$_{0.1}$I$_3$	FTO/c-TiO$_2$/PQDs/spiro-OMeTAD/MoO$_x$/Ag	1.72	16.07	17.58	1.23	0.74	0.207	109
FAPbI$_3$	ITO/SnO$_2$/PQDs/spiro-OMeTAD/Au	1.55	8.38	11.84	1.1	0.64	0.178	26
FAPbI$_3$	FTO/TiO$_2$/PQDs/spiro-OMeTAD/MoO$_x$/Al	1.55	11.6	14.71	1.08	0.73	0.198	90
FAPbI$_3$	ITO/SnO$_2$/PQDs/spiro-OMeTAD/Ag	1.55	12.7	15.40	1.1	0.75	0.178	25
FAPbI$_3$	FTO/TiO$_2$/PQDs/PTAA/MoO$_x$/Ag	1.52	13.2	16.70	1.12	0.71	0.130	40
FAPbI$_3$	FTO/TiO$_2$/PQDs/spiro-OMeTAD/Au	1.55	9.01	11.85	1.12	0.68	0.158	91
FAPbI$_3$	ITO/PEDOT: PSS/PQDs/PCBM/Ag	1.52	10.13	14.56	0.89	0.79	0.360	110

thus circumventing the instability issues caused by the Spiro-OMeTAD. A rational selection is conducted to match the energy level with the PQD film and the HTL; they proved that P3HT, PTB7, and PTB7-Th exhibit a well-aligned energy level to extract the hole while blocking the electrons. As shown in Fig. 9f, the HOMO of the conjugated polymer is almost flushed with the VB of the PQDs, which contributes to the high V_{oc} of 1.28 V (Fig. 9h). Thereafter, to establish the in-depth function of the polymer HTL, they studied the morphology effect of the polymer on the PQD film. As expected, the PQD film with doped Spiro-oMeTAD as the top layer appears to have reduced PL emission and even quenched domains. However, the polymer-covered PQD film preserved homogeneous PL emission quenching, as shown in Fig. 9g. In this study, a reduced V_{oc} loss and enhanced J_{sc} have pushed the PCE to the forefront at that time.

5 Conclusions

In the preceding paragraphs, we discussed the approaches to minimizing V_{oc} loss through defect manipulation, energy

alignment, and device structure optimization. Overcoming V_{oc} loss always plays a prominent role in enhancing photovoltaic performance. Table 1 presents some representative studies with different perovskite compositions and device architectures. We can conclude from Table 1 that the performance of the PQDSCs still lags, probably attributed to the ambiguous relationship between the QDs and device physics. Moreover, the monotonous n–i–p structure is extensively used in PQDSCs, while the development of some novel structures and charge transport materials remains unexploited. Despite the considerable gap between the PQDSCs and the corresponding bulk perovskite solar cells, we reckon that the unique features of PQDs in structure and stability will ensure that they outstand in perovskite photovoltaics. In the following section, we give a brief perspective and attempt to shed some light on the pathway for solving the existing problems.

5.1 Synthesis and ligand manipulation

It has been reported that PQDs still possess larger amounts of defects than bulk perovskites. Because the V_{oc} loss is mostly derived from trap-assisted non-radiative recombination, it is important to manipulate the defect density of the PQDs and

the whole device. Hence, a carefully designed solvent system and rational screening of the ligands are urgently needed. Alternatively, replacing the long-chain ligands with shorter ligands will be an ideal synthesis strategy to obtain the conductive QD precursor and omit further purification, which needs elaborate molecular design and thorough cognition to further optimize the synthesis protocol.[27] Additionally, the surface ligands also contribute to the electronic state and energy levels of the QDs. Simultaneously, the lack of investigation into these questions makes it challenging to design the band structure. Considering the importance of flattened energy levels, it is also essential to pay attention to the size uniformity of the PQDs because the broad size distribution of the PQDs aggravates the energy disorder and causes V_{oc} loss.[12]

5.2 Charge transport materials and device architecture

Charge transport layers play a prominent role in facilitating charge extraction and blocking. The selection of the charge transport layer must also fulfill the criteria that the energy levels are arranged with a type-II alignment. To minimize the V_{oc} loss and achieve better charge carrier management at the interface, the energy offset at the CTL/perovskite interface should be as small as possible. Based on the peculiar properties of the PQDs, wettability, and surface energy will significantly influence the morphology of the upper layers. Thus, exploring various charge transport materials and the interfacial modifier is necessary to further boost the open-circuit voltage and PCE.

The limited film thickness of the PQD film is another limitation in elevating the photovoltaic performance of the PQDSCs.[44] By analyzing the external quantum efficiency (EQE) of the PQDSCs, we can conclude that the film thickness is blamed for serious inadequate light absorption. To overcome this obstacle, the homojunction and heterojunction between perovskite and organic molecules are constructed to induce an extended extent of the built-in electric field.

5.3 Further commercialization and application

The continuous tunability of the bandgap makes it possible for PQDSCs to serve as top cells in tandem solar cells. Moreover, the low fabricating temperature is compatible with processing the flexible device. To demonstrate the large-area device, the as-synthesized PQD ink can also be adapted to slot-die, spray coating, and ink-jet printing. The homogeneity of the large-area PQD film is ensured by the monodispersity and size uniformity of the PQDs. The versatility of PQDs also makes them a promising candidate for semi-transparent solar cells, which tend to be a useful application in building integrated photovoltaics. Overall, it is always worthwhile to study PQD for further embodiment in more optoelectronic devices.

Conflicts of interest

There are no conflicts to declare.

Acknowledgements

References

1 A. Kojima, K. Teshima, Y. Shirai and T. Miyasaka, *J. Am. Chem. Soc.*, 2009, **131**, 6050–6051.

2 H. Min, D. Y. Lee, J. Kim, G. Kim, K. S. Lee, J. Kim, M. J. Paik, Y. K. Kim, K. S. Kim and M. G. J. N. Kim, *Nature*, 2021, **598**, 444–450.

3 M. Kim, J. Jeong, H. Lu, T. K. Lee, F. T. Eickemeyer, Y. Liu, I. W. Choi, S. J. Choi, Y. Jo and H.-B. J. S. Kim, *Science*, 2022, **375**, 302–306.

4 Y. Zhao, F. Ma, Z. Qu, S. Yu, T. Shen, H.-X. Deng, X. Chu, X. Peng, Y. Yuan and X. J. S. Zhang, *Science*, 2022, **377**, 531–534.

5 NREL, Best Research-cell efficiencies, **https://www.nrel.gov/pv/assets/pdfs/best-research-cell-efficiencies-rev220630.pdf**, (accessed December 2022).

6 Y. Qian, Y. Shi, G. Shi, G. Shi, X. Zhang, L. Yuan, Q. Zhong, Y. Liu, Y. Wang, X. Ling, F. Li, M. Cao, S. Li, Q. Zhang, Z. Liu and W. Ma, *Sol. RRL*, 2021, **5**, 2100090.

7 N. Aristidou, C. Eames, I. Sanchez-Molina, X. Bu, J. Kosco, M. S. Islam and S. A. Haque, *Nat. Commun.*, 2017, **8**, 15218.

8 M. Saliba, T. Matsui, J. Y. Seo, K. Domanski, J. P. Correa-Baena, M. K. Nazeeruddin, S. M. Zakeeruddin, W. Tress, A. Abate, A. Hagfeldt and M. Grätzel, *Energy Environ. Sci.*, 2016, **9**, 1989–1997.

9 Z. Li, M. Yang, J. Park, S. Wei, J. J. Berry and K. Zhu, *Chem. Mater.*, 2015, **28**, 284–292.

10 J. A. Christians, P. A. Miranda Herrera and P. V. Kamat, *J. Am. Chem. Soc.*, 2015, **137**, 1530–1538.

11 J. Chen, D. Jia, J. Qiu, R. Zhuang, Y. Hua and X. Zhang, *Nano Energy*, 2022, **96**, 107140.

12 S. Lim, G. Lee, S. Han, J. Kim, S. Yun, J. Lim, Y. Pu, M. J. Ko, T. Park, J. Choi and Y. Kim, *ACS Energy Lett.*, 2021, **6**, 2229–2237.

13 A. Swarnkar, A. R. Marshall, E. M. Sanehira, B. D. Chernomordik, D. T. Moore, J. A. Christians, T. Chakrabarti and J. M. J. S. Luther, *Science*, 2016, **354**, 92–95.

14 F. Liu, Y. Zhang, C. Ding, S. Kobayashi, T. Izuishi, N. Nakazawa, T. Toyoda, T. Ohta, S. Hayase, T. Minemoto, K. Yoshino, S. Dai and Q. Shen, *ACS Nano*, 2017, **11**, 10373–10383.

15 F. Krieg, S. T. Ochsenbein, S. Yakunin, S. ten Brinck, P. Aellen, A. Suess, B. Clerc, D. Guggisberg, O. Nazarenko, Y. Shynkarenko, S. Kumar, C. J. Shih, I. Infante and M. V. Kovalenko, *ACS Energy Lett.*, 2018, **3**, 641–646.

16 C. Bi, Z. Yao, X. Sun, X. Wei, J. Wang and J. Tian, *Adv. Mater.*, 2021, **33**, e2006722.

17 L. C. Schmidt, A. Pertegas, S. Gonzalez-Carrero, O. Malinkiewicz, S. Agouram, G. Mínguez Espallargas, H. J. Bolink, R. E. Galian and J. Perez-Prieto, *J. Am. Chem. Soc.*, 2014, **136**, 850–853.

18 O. Vybornyi, S. Yakunin and M. V. Kovalenko, *Nanoscale*, 2016, **8**, 6278–6283.

19 X. Li, Y. Wu, S. Zhang, B. Cai, Y. Gu, J. Song and H. Zeng, *Adv. Funct. Mater.*, 2016, **26**, 2435–2445.

20 J. Shamsi, A. S. Urban, M. Imran, L. De Trizio and L. Manna, *Chem. Rev.*, 2019, **119**, 3296–3348.

21 G. H. Ahmed, J. Yin, R. Bose, L. Sinatra, E. Alarousu, E. Yengel, N. M. AlYami, M. I. Saidaminov, Y. Zhang, M. N. Hedhili, O. M. Bakr, J. Brédas and O. F. Mohammed, *Chem. Mater.*, 2017, **29**, 4393–4400.

22 L. Protesescu, S. Yakunin, M. I. Bodnarchuk, F. Krieg, R. Caputo, C. H. Hendon, R. X. Yang, A. Walsh and M. V. Kovalenko, *Nano Lett.*, 2015, **15**, 3692–3696.

23 J. Yuan, X. Ling, D. Yang, F. Li, S. Zhou, J. Shi, Y. Qian, J. Hu, Y. Sun, Y. Yang, X. Gao, S. Duhm, Q. Zhang and W. Ma, *Joule*, 2018, **2**, 2450–2463.

24 Q. Zhao, A. Hazarika, X. Chen, S. P. Harvey, B. W. Larson, G. R. Teeter, J. Liu, T. Song, C. Xiao, L. Shaw, M. Zhang, G. Li, M. C. Beard and J. M. Luther, *Nat. Commun.*, 2019, **10**, 2842.

25 J. Xue, R. Wang, L. Chen, S. Nuryyeva, T. H. Han, T. Huang, S. Tan, J. Zhu, M. Wang, Z. K. Wang, C. Zhang, J. W. Lee and Y. Yang, *Adv. Mater.*, 2019, **31**, e1900111.

26 J. Xue, J. Lee, Z. Dai, R. Wang, S. Nuryyeva, M. E. Liao, S. Chang, L. Meng, D. Meng, P. Sun, O. Lin, M. S. Goorsky and Y. Yang, *Joule*, 2018, **2**, 1866–1878.

27 X. Ling, J. Yuan and W. Ma, *Acc. Mater. Res.*, 2022, **3**, 866–878.

28 J. Chen, D. Jia, R. Zhuang, Y. Hua and X. Zhang, *Adv. Mater.*, 2022, **34**, e2204259.

29 F. Li, S. Zhou, J. Yuan, C. Qin, Y. Yang, J. Shi, X. Ling, Y. Li and W. Ma, *ACS Energy Lett.*, 2019, **4**, 2571–2578.

30 Q. Wang, Z. Jin, D. Chen, D. Bai, H. Bian, J. Sun, G. Zhu, G. Wang and S. F. Liu, *Adv. Energy Mater.*, 2018, **8**, 180007.

31 D. Jia, J. Chen, M. Yu, J. Liu, E. M. J. Johansson, A. Hagfeldt and X. Zhang, *Small*, 2020, **16**, e2001772.

32 X. Zhang, H. Huang, Y. M. Maung, J. Yuan and W. Ma, *Chem. Commun.*, 2021, **57**, 7906–7909.

33 L. Hu, Q. Zhao, S. Huang, J. Zheng, X. Guan, R. Patterson, J. Kim, L. Shi, C. H. Lin, Q. Lei, D. Chu, W. Tao, S. Cheong, R. D. Tilley, A. W. Y. Ho-Baillie, J. M. Luther, J. Yuan and T. Wu, *Nat. Commun.*, 2021, **12**, 466.

34 Y. K. Wang, K. Singh, J. Y. Li, Y. Dong, X. Q. Wang, J. M. Pina, Y. J. Yu, R. Sabatini, Y. Liu, D. Ma, J. Liu, Z. Liu, Y. Gao, O. Voznyy, W. Ma, M. K. Fung, L. S. Liao and E. H. Sargent, *Adv. Mater.*, 2022, **34**, e2200854.

35 D. Jia, J. Chen, X. Mei, W. Fan, S. Luo, M. Yu, J. Liu and X. Zhang, *Energy Environ. Sci.*, 2021, **14**, 4599–4609.

36 E. M. Sanehira, A. R. Marshall, J. A. Christians, S. P. Harvey, P. N. Ciesielski, L. M. Wheeler, P. Schulz, L. Y. Lin, M. C. Beard and J. M. Luther, *Sci. Adv.*, 2017, **3**, eaao4204.

37 X. Ling, S. Zhou, J. Yuan, J. Shi, Y. Qian, B. W. Larson, Q. Zhao, C. Qin, F. Li, G. Shi, C. Stewart, J. Hu, X. Zhang, J. M. Luther, S. Duhm and W. Ma, *Adv. Energy Mater.*, 2019, **9**, 1900721.

38 M. Hao, Y. Bai, S. Zeiske, L. Ren, J. Liu, Y. Yuan, N. Zarrabi, N. Cheng, M. Ghasemi, P. Chen, M. Lyu, D. He, J. Yun, Y. Du, Y. Wang, S. Ding, A. Armin, P. Meredith, G. Liu, H. Cheng and L. Wang, *Nat. Energy*, 2020, **5**, 79–88.

39 L. Liu, A. Najar, K. Wang, M. Du and S. F. Liu, *Adv. Sci.*, 2022, **9**, e2104577.

40 K. Ji, J. Yuan, F. Li, Y. Shi, X. Ling, X. Zhang, Y. Zhang, H. Lu, J. Yuan and W. Ma, *J. Mater. Chem. A*, 2020, **8**, 8104–8112.

41 D. Jia, J. Chen, J. Qiu, H. Ma, M. Yu, J. Liu and X. Zhang, *Joule*, 2022, **6**, 1632–1653.

42 M. I. Bodnarchuk, S. C. Boehme, S. Ten Brink, C. Bernasconi, Y. Shynkarenko, F. Krieg, R. Widmer, B. Aeschlimann, D. Gunther, M. V. Kovalenko and I. Infante, *ACS Energy Lett.*, 2019, **4**, 63–74.

43 W. Shockley and H. J. Queisser, *J. Appl. Phys.*, 1961, **32**, 510–519.

44 X. Zhang, H. Huang, X. Ling, J. Sun, X. Jiang, Y. Wang, D. Xue, L. Huang, L. Chi, J. Yuan and W. Ma, *Adv. Mater.*, 2022, **34**, e2105977.

45 S. Seth, T. Ahmed, A. De and A. Samanta, *ACS Energy Lett.*, 2019, **4**, 1610–1618.

46 W. Tress, *Adv. Energy Mater.*, 2017, **7**, 1602358.

47 W. Wei, W. Chen, X. Zhao, Z. Yang and Y. Liu, *J. Alloys Compd.*, 2022, **891**, 161985.

48 M. Stolterfoht, P. Caprioglio, C. M. Wolff, J. A. Márquez, J. Nordmann, S. Zhang, D. Rothhardt, U. Hörmann, Y. Amir, A. Redinger, L. Kegelmann, F. Zu, S. Albrecht, N. Koch, T. Kirchartz, M. Saliba, T. Unold and D. Neher, *Energy Environ. Sci.*, 2019, **12**, 2778–2788.

49 J. P. Correa Baena, L. Steier, W. Tress, M. Saliba, S. Neutzner, T. Matsui, F. Giordano, T. J. Jacobsson, A. R. Srimath Kandada, S. M. Zakeeruddin, A. Petrozza, A. Abate, M. K. Nazeeruddin, M. Grätzel and A. Hagfeldt, *Energy Environ. Sci.*, 2015, **8**, 2928–2934.

50 J. Correa-Baena, W. Tress, K. Domanski, E. H. Anaraki, S.-H. Turren-Cruz, B. Roose, P. P. Boix, M. Grätzel, M. Saliba, A. Abate and A. Hagfeldt, *Energy Environ. Sci.*, 2017, **10**, 1207–1212.

51 W. Yang, Y. Yao and C. Wu, *J. Appl. Phys.*, 2015, **117**, 095502.

52 D. Ompong, K. S. Ram, D. D. Y. Setsoafia, H. Mehdizadeh Rad and J. Singh, *Adv. Mater. Interfaces*, 2022, **10**, 2201578.

53 K. Chen, W. Jin, Y. Zhang, T. Yang, P. Reiss, Q. Zhong, U. Bach, Q. Li, Y. Wang, H. Zhang, Q. Bao and Y. Liu, *J. Am. Chem. Soc.*, 2020, **142**, 3775–3783.

54 J. Yuan, C. Bi, J. Xi, R. Guo and J. Tian, *J. Phys. Chem. Lett.*, 2021, **12**, 1018–1024.

55 D. Yang, X. Li, W. Zhou, S. Zhang, C. Meng, Y. Wu, Y. Wang and H. Zeng, *Adv. Mater.*, 2019, **31**, e1900767.

56 Q. A. Akkerman, T. P. Nguyen, S. C. Boehme, F. Montanarella, D. N. Dirin, P. Wechsler, F. Beiglböck, G. Rainò, R. Erni, C. Katan, J. Even and M. V. Kovalenko, *Science*, 2022, **377**, 1406–1412.

57 U. Rau, B. Blank, T. C. Müller and T. Kirchartz, *Phys. Rev. Appl.*, 2017, **7**, 044016.

58 K. Vandewal, K. Tvingstedt, A. Gadisa, O. Inganäs and J. V. Manca, *Phys. Rev. B: Condens. Matter Mater. Phys.*, 2010, **81**, 125204.

59 U. Rau, *Phys. Rev. B: Condens. Matter Mater. Phys.*, 2007, **76**, 085303.

60 J.-F. Guillemoles, T. Kirchartz, D. Cahen and U. Rau, *Nat. Photonics*, 2019, **13**, 501–505.

61 J. Yao, T. Kirchartz, M. S. Vezie, M. A. Faist, W. Gong, Z. He, H. Wu, J. Troughton, T. Watson, D. Bryant and J. Nelson, *Phys. Rev. Appl.*, 2015, **4**, 0141020.

62 S. Liu, J. Yuan, W. Deng, M. Luo, Y. Xie, Q. Liang, Y. Zou, Z. He, H. Wu and Y. Cao, *Nat. Photonics*, 2020, **14**, 300–305.

63 J. Kang and L. W. Wang, *J. Phys. Chem. Lett.*, 2017, **8**, 489–493.

64 M. A. Boles, D. Ling, T. Hyeon and D. V. Talapin, *Nat. Mater.*, 2016, **15**, 364.

65 Y. Bai, M. Hao, S. Ding, P. Chen and L. Wang, *Adv. Mater.*, 2022, **34**, e2105958.

66 G. R. Yettapu, D. Talukdar, S. Sarkar, A. Swarnkar, A. Nag, P. Ghosh and P. Mandal, *Nano Lett.*, 2016, **16**, 4838–4848.

67 Y. Chen, S. R. Smock, A. H. Flintgruber, F. A. Perras, R. L. Brutchey and A. J. Rossini, *J. Am. Chem. Soc.*, 2020, **142**, 6117–6127.

68 G. Nedelcu, L. Protesescu, S. Yakunin, M. I. Bodnarchuk, M. J. Grotevent and M. V. Kovalenko, *Nano Lett.*, 2015, **15**, 5635–5640.

69 T. He, S. Li, Y. Jiang, C. Qin, M. Cui, L. Qiao, H. Xu, J. Yang, R. Long, H. Wang and M. Yuan, *Nat. Commun.*, 2020, **11**, 1672.

70 Q. Jiang, J. Tong, Y. Xian, R. A. Kerner, S. P. Dunfield, C. Xiao, R. A. Scheidt, D. Kuciauskas, X. Wang, M. P. Hautzinger, R. Tirawat, M. C. Beard, D. P. Fenning, J. J. Berry, B. W. Larson, Y. Yan and K. Zhu, *Nature*, 2022, **611**, 278–283.

71 C. Xu, S. Zhang, W. Fan, F. Cheng, H. Sun, Z. Kang and Y. Zhang, *Adv. Mater.*, 2022, e2207172, DOI: 10.1002/adma.202207172.

72 H. Chen, Y. Wang, Y. Fan, Y. Chen, Y. Miao, Z. Qin, X. Wang, X. Liu, K. Zhu, F. Gao and Y. Zhao, *Natl. Sci. Rev.*, 2022, **9**, nwac127.

73 R. Chen, S. Liu, X. Xu, F. Ren, J. Zhou, X. Tian, Z. Yang, X. Guanz, Z. Liu, S. Zhang, Y. Zhang, Y. Wu, L. Han, Y. Qi and W. Chen, *Energy Environ. Sci.*, 2022, **15**, 2567–2580.

74 S. Gharibzadeh, P. Fassl, I. M. Hossain, P. Rohrbeck, M. Frericks, M. Schmidt, T. Duong, M. R. Khan, T. Abzieher, B. A. Nejand, F. Schackmar, O. Almora, T. Feeney, R. Singh, D. Fuchs, U. Lemmer, J. P. Hofmann, S. A. L. Weber and U. W. Paetzold, *Energy Environ. Sci.*, 2021, **14**, 5875–5893.

75 Y. Cui, J. Shi, F. Meng, B. Yu, S. Tan, S. He, C. Tan, Y. Li, H. Wu, Y. Luo, D. Li and Q. Meng, *Adv. Mater.*, 2022, **34**, e2205028.

76 Y. Che, Z. Liu, Y. Duan, J. Wang, S. Yang, D. Xu, W. Xiang, T. Wang, N. Yuan, J. Ding and S. F. Liu, *Angew Chem., Int. Ed.*, 2022, **61**, e202205012.

77 J. J. S. Owen, *Science*, 2015, **347**, 615–616.

78 J. Wong, S. T. Omelchenko and H. A. Atwater, *ACS Energy Lett.*, 2020, **6**, 52–57.

79 D. Zhitomirsky, I. J. Kramer, A. J. Labelle, A. Fischer, R. Debnath, J. Pan, O. M. Bakr and E. H. Sargent, *Nano Lett.*, 2012, **12**, 1007–1012.

80 Q. A. Akkerman, G. Raino, M. V. Kovalenko and L. Manna, *Nat. Mater.*, 2018, **17**, 394–405.

81 J. Yuan, C. Bi, S. Wang, R. Guo, T. Shen, L. Zhang and J. Tian, *Adv. Funct. Mater.*, 2019, **29**, 1906615.

82 L. M. Wheeler, E. M. Sanehira, A. R. Marshall, P. Schulz, M. Suri, N. C. Anderson, J. A. Christians, D. Nordlund, D. Sokaras, T. Kroll, S. P. Harvey, J. J. Berry, L. Y. Lin and J. M. Luther, *J. Am. Chem. Soc.*, 2018, **140**, 10504–10513.

83 J. W. Lee, H. S. Kim and N. G. Park, *Acc. Chem. Res.*, 2016, **49**, 311–319.

84 K. Hoshi, T. Chiba, J. Sato, Y. Hayashi, Y. Takahashi, H. Ebe, S. Ohisa and J. Kido, *ACS Appl. Mater. Interfaces*, 2018, **10**, 24607–24612.

85 T. Chiba, Y. Hayashi, H. Ebe, K. Hoshi, J. Sato, S. Sato, Y.-J. Pu, S. Ohisa and J. Kido, *Nat. Photonics*, 2018, **12**, 681–687.

86 J. Kim, B. Koo, W. H. Kim, J. Choi, C. Choi, S. J. Lim, J. Lee, D. Kim, M. J. Ko and Y. Kim, *Nano Energy*, 2019, **66**, 104130.

87 R. Azmi, S. Sinaga, H. Aqoma, G. Seo, T. K. Ahn, M. Park, S. Ju, J. Lee, T.-W. Kim, S. Oh and S. Jang, *Nano Energy*, 2017, **39**, 86–94.

88 X. Ling, J. Yuan, X. Zhang, Y. Qian, S. M. Zakeeruddin, B. W. Larson, Q. Zhao, J. Shi, J. Yang, K. Ji, Y. Zhang, Y. Wang, C. Zhang, S. Duhm, J. M. Luther, M. Grätzel and W. Ma, *Adv. Mater.*, 2020, **32**, e2001906.

89 C. H. Chuang, P. R. Brown, V. Bulovic and M. G. Bawendi, *Nat. Mater.*, 2014, **13**, 796–801.

90 M. Suri, A. Hazarika, B. W. Larson, Q. Zhao, M. Vallés-Pelarda, T. D. Siegler, M. K. Abney, A. J. Ferguson, B. A. Korgel and J. M. Luther, *ACS Energy Lett.*, 2019, **4**, 1954–1960.

91 A. Hazarika, Q. Zhao, E. A. Gaulding, J. A. Christians, B. Dou, A. R. Marshall, T. Moot, J. J. Berry, J. C. Johnson and J. M. Luther, *ACS Nano*, 2018, **12**, 10327–10337.

92 Q. Zhao, A. Hazarika, L. T. Schelhas, J. Liu, E. A. Gaulding, G. Li, M. Zhang, M. F. Toney, P. C. Sercel and J. M. Luther, *ACS Energy Lett.*, 2019, **5**, 238–247.

93 J. Liu, K. Xian, L. Ye and Z. Zhou, *Adv. Mater.*, 2021, **33**, e2008115.

94 J. Qing, X. Liu, M. Li, F. Liu, Z. Yuan, E. Tiukalova, Z. Yan, M. Duchamp, S. Chen, Y. Wang, S. Bai, J. Liu, H. J. Snaith, C. Lee, T. C. Sum and F. Gao, *Adv. Energy Mater.*, 2018, **8**, 1800185.

95 C. Xiao, Q. Zhao, C. Jiang, Y. Sun, M. M. Al-Jassim, S. U. Nanayakkara and J. M. Luther, *Nano Energy*, 2020, **78**, 105319.

96 J. Yuan, A. Gallagher, Z. Liu, Y. Sun and W. Ma, *J. Mater. Chem. A*, 2015, **3**, 2572–2579.

97 I. Gelmetti, N. F. Montcada, A. Pérez-Rodríguez, E. Barrena, C. Ocal, I. García-Benito, A. Molina-Ontoria, N. Martín, A. Vidal-Ferran and E. Palomares, *Energy Environ. Sci.*, 2019, **12**, 1309–1316.

98 S. Lim, J. Kim, J. Y. Park, J. Min, S. Yun, T. Park, Y. Kim and J. Choi, *ACS Appl. Mater. Interfaces*, 2021, **13**, 6119–6129.

99 H. Yang, Y. Shen, R. Zhang, Y. Wu, W. Chen, F. Yang, Q. Cheng, H. Chen, X. Ou, H. Yang, F. Gao, Y. Li and Y. Li, *Adv. Energy Mater.*, 2022, **12**, 2202207.

100 F. Lamberti, T. Gatti, E. Cescon, R. Sorrentino, A. Rizzo, E. Menna, G. Meneghesso, M. Meneghetti, A. Petrozza and L. Franco, *Chem*, 2019, **5**, 1806–1817.

101 J. Y. Seo, S. Akin, M. Zalibera, M. A. R. Preciado, H. S. Kim, S. M. Zakeeruddin, J. V. Milić and M. Grätzel, *Adv. Funct. Mater.*, 2021, **31**, 2102124.

102 S. Wang, Q. Wei, K. Wang, Z. Zhang, D. Zhao, C. Liang, T. Liu, J. Guo, C. Su, Y. Li and G. Xing, *Small*, 2020, **16**, e1907513.

103 C. Ding, R. Huang, C. Ahläng, J. Lin, L. Zhang, D. Zhang, Q. Luo, F. Li, R. Österbacka and C. Ma, *J. Mater. Chem. A*, 2021, **9**, 7575–7585.

104 T. Zhang, F. Wang, H. Kim, I. Choi, C. Wang, E. Cho, R. Konefal, Y. Puttisong, K. Terado and L. J. S. Kobera, *Science*, 2022, **377**, 495–501.

105 Q. A. Akkerman, M. Gandini, F. Di Stasio, P. Rastogi, F. Palazon, G. Bertoni, J. M. Ball, M. Prato, A. Petrozza and L. Manna, *Nat. Energy*, 2016, **2**, 16194.

106 Y. Shi, L. Yuan, Z. Liu, Y. Lu, B. Yuan, W. Shen, B. Xue, Y. Zhang, Y. Qian, F. Li, X. Zhang, Y. Liu, Y. Wang, L. Wang, J. Yuan, L. S. Liao, B. Yang, Y. Yu and W. Ma, *ACS Nano*, 2022, **16**, 10534–10544.

107 D. Ghosh, M. Y. Ali, D. K. Chaudhary and S. Bhattacharyya, *Sol. Energy Mater. Sol. Cells*, 2018, **185**, 28–35.

108 Y. Liu, Q. Li, W. Zhang, Z. Yang, S. Zhao and W. Chen, *ACS Appl. Energy Mater.*, 2021, **4**, 6688–6696.

109 L. Zhang, C. Kang, G. Zhang, Z. Pan, Z. Huang, S. Xu, H. Rao, H. Liu, S. Wu, X. Wu, X. Li, Z. Zhu, X. Zhong and A. K. Y. Jen, *Adv. Funct. Mater.*, 2020, **31**, 2005930.

110 Y. Xu, H. Li, S. Ramakrishnan, D. Song, Y. Zhang, M. Cotlet and Q. Yu, *ACS Appl. Energy Mater.*, 2022, **5**, 9858–9869.

111 P. Wurfel, *J. Phys. C: Solid State Phys.*, 1982, **15**, 3967.

112 M. Stolterfoht, C. M. Wolff, J. A. Márquez, S. Zhang, C. J. Hages, D. Rothhardt, S. Albrecht, P. L. Burn, P. Meredith, T. Unold and D. Neher, *Nat. Energy*, 2018, **3**, 847–854.

113 S. Wang, P. Wang, B. Chen, R. Li, N. Ren, Y. Li, B. Shi, Q. Huang, Y. Zhao, M. Grätzel and X. Zhang, *eScience*, 2022, **2**, 339–346.